Jnl of Modern Optics

Topical review Self-written waveguides
Catching light in its own trap

Tanya M. Monro[1], C. Martijn de Sterke[2,3], and L. Poladian[3]
Optoelectronics Research Centre
University of Southampton, SO17 1BJ, UK[1]
School of Physics, University of Sydney,
NSW 2006 Australia[2]
Australian Photonics CRC, University of Sydney,
Australian Technology Park, NSW 1430, Australia [3].

April 4, 2000

Abstract

Self-written structures form dynamically in photosensitive media, in which the refractive index changes permanently under the influence of light that propagates through it. Self-written waveguides have been observed in a variety of materials including glasses and polymers. Detailed theoretical analysis of self-writing in germanosilicate glasses is in good agreement with experiments. We review recent experimental and theoretical progress in this field and indicate likely areas of future progress.

1 Introduction

1.1 Overview of self-writing

Consider a Gaussian beam incident on a uniform planar waveguide, as sketched in Fig. 1.1(a). The beam initially diffracts in the plane of the waveguide, as sketched by the solid lines, and the intensity is highest on the propagation axis. A wide range of materials experience long-lasting refractive index changes in response to illumination at specific wavelengths. This "photosensitivity" produces the largest changes in refractive index where the intensity is high, and so the largest changes also occur on the propagation axis. Although the index can sometimes decrease, we consider here only positive changes (see Section 1.2). Hence the beam initially diffracts, but forms a region of raised refractive index along the propagation axis. This reduces its diffraction, and the beam begins to be confined to the channel it has created. If the writing beam is left on, over time the refractive index distribution evolves into a fairly uniform channel waveguide along the propagation axis. A sketch of how the writing beam

becomes guided by the waveguide it creates in the photosensitive material is shown in Fig. 1(b). This is a *self-written waveguide* because the beam of light that creates the waveguide is subsequently guided by it.

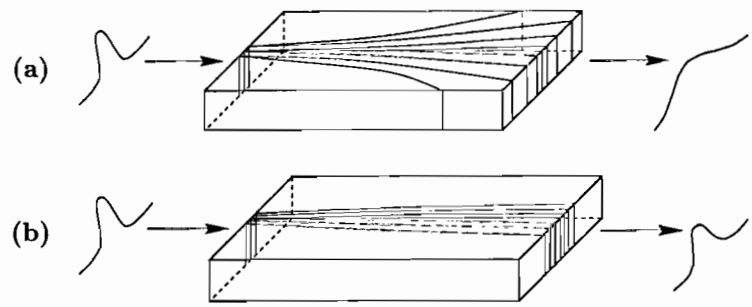

Figure 1: (a) A beam incident on a photosensitive planar waveguide initially diffracts, as sketched, and the refractive index begins to change in response to this illumination. (b) Over time the beam is guided by the waveguide it has *self-written* in the glass.

The self-writing process described above is not restricted to the planar waveguide geometry described above, and waveguides can also be self-written in bulk photosensitive materials which initially have a spatially uniform refractive index distribution. Although the details in the evolution of the waveguide differ somewhat, a single-peaked input beam can again be used to form a channel in bulk photosensitive material.

Self-writing is a relatively new area of research; the first experiment was done in 1993 by Frisken [1] in UV-cured epoxy, and since then self-writing has been observed in a range of materials (see Section 6). Self-written waveguides have a number of advantages over waveguides written using more conventional techniques such as reactive ion etching or photolithography. In surface waveguides, roughness can lead to large scattering losses, which can be significantly reduced by using buried waveguides [2]. However, many processing steps are needed to form buried waveguides using conventional techniques. In contrast, if the buffer layer is transparent at the writing wavelength, direct writing can be used to form waveguides in a buried planar waveguide. The direct writing of waveguides also have the advantage that no chemical processing is necessary and they can be formed with commonly available lasers. Self-writing possesses all the advantages of photosensitive direct writing: waveguides can be written directly in buried planar waveguides. Self-writing also has additional advantages; for example, the simulations in Section 3 predict that self-written waveguides typically have no sharp features, which reduces the scattering losses. Also, it is potentially possible to form a complex waveguiding structure by tailoring the writing beam.

The self-writing process that has been investigated in most detail uses germanium doped glass, and in Section 1.2 we briefly review glass photosensitivity. As most applications of integrated photonics devices use silica-on-silicon

waveguides, glass waveguides are more likely to be easily integrated than other materials.

1.2 Photosensitivity in glass

In 1977, Hill *et al.* [3] launched 488 nm light into a germanium-doped optical fibre. On the time-scale of a minute, the fibre reflectivity increased over a narrow frequency band. Hill proposed that the fibre core is *photosensitive*, meaning that the refractive index increases in response to illumination, changing most where the intensity is highest. In this experiment, the incident light interferes with the light that is Fresnel reflected at the fibre end, forming a periodic intensity distribution. Photosensitivity leads to the patterning of a grating in the core. The observed narrow spectral response is consistent with the formation of a grating. Such *Hill gratings* are *self-written*, because the light is reflected by the grating it creates.

Lam *et al.* [4] showed that photosensitivity at 488 nm is a two-photon absorption process. Following this, Meltz *et al.* [5] suggested that germanosilicate glass should be highly photosensitive at the corresponding one-photon wavelength of 244 nm. They *externally* exposed the side of a germanium-doped fibre to two interfering plane waves at 244 nm. This forms a periodic intensity distribution in the core, and so a grating is imprinted via photosensitivity. Using external writing, index changes of up to $\Delta n = 3 \times 10^{-5}$ can be obtained in fibres with $2-4\,\%$ GeO_2 [5], and the magnitude of Δn is nearly constant over a broad wavelength range [6].

Germanosilicate planar waveguides are also photosensitive, which is particularly useful in integrated optics, as complex waveguide structures cannot be easily adapted to the fibre geometry [7]. Photosensitivity has been used to pattern gratings directly in planar germanosilicate waveguides formed by Plasma Enhanced Chemical Vapour Deposition (PECVD) [8, 9]. This was done by externally exposing the waveguide to a modulated intensity distribution using a phase mask. Using 193 nm light, index increases as large as $\Delta n = 2.5 \times 10^{-3}$ have been induced, and similar changes are obtained at 244 nm [7]. Chalcogenide glasses such as As_2S_3 are an area of recent interest because very large photosensitive refractive index changes can be achieved in these materials (Tanaka *et al.* [10] report $\Delta n = 10^{-2}$). It should be possible to create self-written waveguides in any material which experiences long-lasting increases in refractive index in response to illumination.

Hill *et al.* originally noted that photosensitivity is crucially dependent on the presence of germanium in the core. However, in 1991 it was found that other dopants can also lead to photosensitivity [11, 12]. It is thought that dopants form absorption bands which allow energy to be coupled into the glass matrix. Although it is thought that the resulting refractive index change results from mechanisms that occur due to this coupling [13], these mechanisms are not completely understood. The details of the photosensitivity mechanism are not discussed in this review (see for example the review by Douay *et al.* [14] for a comprehensive review of photosensitivity and photosensitivity mechanisms).

Photosensitive refractive index changes in glass are long lasting, and although heating accelerates the aging of photosensitive index changes, for practical purposes they can be considered to be effectively permanent. For example, at room temperature a grating with an initial reflectivity of 90% experiences a decay in reflectivity of 1% in the first nine hours, and only another 1% over the next 1000 years [15]. This permanency is the main reason why self-writing differs from self-action effects such as photorefractive or spatial solitons (see Section 6.6).

1.3 Outline of this review

Self-writing has now been observed in a range of light-sensitive materials, and this review begins by describing the model that has been developed to explore self-writing processes. Although the microscopic details of the index change mechanisms vary significantly between the different materials used in these self-writing experiments, the simple phenomenological model described in Section 2 can be adapted to apply to a broad range of materials.

Section 3 describes numerical simulations which are based on this phenomenological model of self-writing. These simulations reveal that even the formation of a simple channel is a rich and complex dynamical problem. By altering the form of the writing beam, the theoretical work predicts that it is possible to create other more complicated waveguide structures. Section 4 reviews a range of theoretical techniques which have been developed to investigate the details of the self-writing process.

The self-writing process that has been investigated most fully makes use of a two-photon photosensitivity process in germanosilicate planar waveguides (see Section 1.2), and this experimental work is described in Section 5. A range of related self-writing processes have been observed in other light-sensitive materials, and this work is described in Section 6.

2 Modelling self-writing

In this section a phenomenological model for self-writing is described. As this model does not depend on any microscopic details of the photosensitivity process, it should also apply to other materials well.

2.1 Geometries

Bulk materials In a bulk geometry, the refractive index is initially taken to be uniform throughout. This geometry is shown in Fig. 2(a), where z points in the propagation direction, and the transverse coordinates are x and y. The solid lines sketch the initial diffraction of a beam incident from the left.

The electric field ($\vec{\mathcal{E}}$) is taken to be monochromatic with frequency ω. The light is taken to be linearly polarised in the x-direction, say, and so

$$\vec{\mathcal{E}}(x,y,z,t) = \exp[i\,(n_0 k_0 z - \omega t)]\;\mathcal{E}(x,y,z,t)\,\hat{x} + c.c. \qquad (1)$$

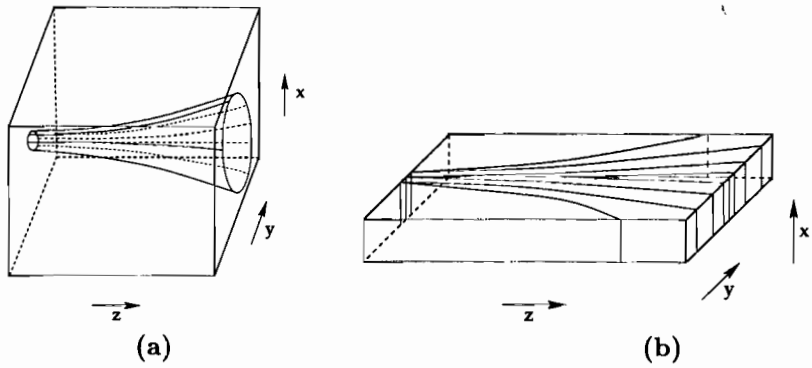

Figure 2: Diffraction of a single-peaked beam in (a) bulk and (b) planar geometries.

where $\mathcal{E}$ is the electric field envelope amplitude, n_0 is the refractive index in the unexposed structure and $k_0 = \omega/c$ is the free space wavenumber.

Planar waveguide The planar waveguide geometry is shown in Fig. 2(b); light is confined to the plane in the x-direction, and the refractive index is initially uniform in the plane formed by the z- and y-axes.

The light is taken to be in a TM mode of the planar structure, and is again taken to be monochromatic, so

$$\vec{\mathcal{E}}(x,y,z,t) = \exp[i\,(n_0 k_0 z - \omega t)]\;\vec{F}(x)\;\mathcal{E}(y,z,t) + c.c. \tag{2}$$

where $\vec{F}(x)$, the modal field profile, which has $\hat{x}$ and $\hat{z}$ components. In the weak-guidance approximation, the $\hat{z}$-component can be ignored, and this is done here. The TM mode is chosen to correspond to the experiment in Section 5, and $\vec{F}(x)$ is normalized such that the intensity can be written as $I = \mathcal{E}\mathcal{E}^*$ [16].

The photosensitive index changes that we consider here are small compared with the index difference between the guiding layer and the surrounding layers. Observations in Section 5 support this: the index step in the x-direction is 2.2×10^{-2}, whereas the photosensitive index change saturates at $\approx 10^{-3}$. Hence $\vec{F}(x)$ is virtually unaffected by the photosensitive index changes, and only one transverse dimension, y, remains.

2.2 Description of light propagation

In general, light propagation is described by the vector wave equation. However, if the beam varies only slowly under propagation, then the paraxial approximation can be used. Substituting Eq. (1) or Eq. (2) into the wave equation [17],

$$\frac{1}{2}\frac{\partial^2 \mathcal{E}}{\partial z^2} + ik_0 n_0 \frac{\partial \mathcal{E}}{\partial z} + \frac{1}{2}\nabla_t^2 \mathcal{E} + k_0^2 n_0 \Delta n \mathcal{E} + k_0^2 \Delta n^2 \mathcal{E} = 0, \tag{3}$$

where $\Delta n = n(x,y,z,t) - n(x,y,z,0)$ and $n(x,y,z,t)$ is the refractive index deviation from n at time t, which is generally complex. In a bulk geometry,

$\mathcal{E} = \mathcal{E}(x, y, z, t)$, and $\nabla_t^2 = \frac{\partial^2}{\partial x^2} + \frac{\partial^2}{\partial y^2}$. In a planar geometry, $\mathcal{E} = \mathcal{E}(y, z, t)$, and $\nabla_t^2 = \frac{\partial^2}{\partial y^2}$ and we assume that the field and index profiles are unaffected in the x-direction [18]. In the planar geometry, the index change is averaged over x:

$$\Delta n(y, z, t) = \frac{\int_{-\infty}^{\infty} |\hat{F}(x)|^2 \, \Delta n(x, y, z, t) \, dx}{\int_{-\infty}^{\infty} |\hat{F}(x)|^2 \, dx}, \tag{4}$$

a technique that is also used in the *effective index method* [17].

The paraxial approximation implies that the beam varies slowly with z, and so the first term in Eq. (3) is negligible [19], and as Δn is small, the last term can also be ignored. Hence the *paraxial wave equation* is [18, 19]

$$ik_0 n_0 \frac{\partial \mathcal{E}}{\partial z} + \frac{1}{2}\nabla_t^2 \mathcal{E} + k_0^2 n_0 \Delta n \mathcal{E} + \frac{i}{2} k_0 n_0 \alpha \mathcal{E} = 0. \tag{5}$$

where the Δn is now taken to be real, and losses have been written explicitly; α is the attenuation coefficient leading to a loss in dB per unit length of $4.343\,\alpha$. The first term in Eq. (5) describes propagation, the second diffraction, the third accounts for how photosensitive refractive index changes affect light propagation, and the last describes the effect of material loss. We refer to Section 2.3.2 for a discussion of modelling the material loss.

In the experiment in Section 5, a Gaussian writing beam is incident on the *input face* ($z = 0$). Hence the initial conditions are

$$\mathcal{E}(y, 0, t) = \mathcal{E}_0 \, \exp\Big(-y^2/a^2\Big), \quad \mathcal{E}(x, y, 0, t) = \mathcal{E}_0 \, \exp\Big(-(x^2 + y^2)/a^2\Big) \tag{6}$$

for planar and bulk materials respectively, where a is the beam width, corresponding to a full width at half maximum (FWHM) of $\sqrt{2 \ln 2}\, a$ in the intensity. For this profile, the paraxial approximation is valid when $a \gg \lambda/(2\pi)$ (otherwise the beam diffracts too rapidly). Note that for these Gaussian beams the Rayleigh range is [16]

$$z_R = k_0 n_0 a^2/2. \tag{7}$$

2.3 Modelling light-induced changes

2.3.1 Photosensitivity

When 488 nm light is used, the induced index change is proportional to the squared writing power [4, 20], which suggests the local two-photon model [21, 22]

$$\frac{\partial \Delta n}{\partial t} = A I^2. \tag{8}$$

where $I(z, t)$ is the local light intensity and A depends on material properties [21]. Typically the index increases ($A > 0$) [22]. Eq. (8) is a *local* model because the index change only depends on the history of the illumination at that position. Eq. (8) contains the ingredients necessary to describe the Hill grating results

[21]. However it cannot be completely correct, as the index increases without bound, which is clearly unphysical.

By analogy with Eq. (8), it might be expected that the one-photon model

$$\frac{\partial \Delta n}{\partial t} \propto I, \tag{9}$$

should describe photosensitivity at 244 nm well. Indeed, Krug *et al.* [23] showed that it can give good agreement with data. However, photosensitivity at 244 nm seems to be rather more complex than at 488 nm, and it is not clear at present how best to describe photosensitivity at 244 nm. Different materials, fabrication techniques, and even different writing wavelengths produce noticeable differences to the photosensitivity of germanosilicate glass.

2.3.2 Other light-induced changes

The model as described thus far gives qualitative agreement with experiment, both when losses are ignored [24, 25, 26] and when uniform, constant losses are included [27]. However, in either case, the model's quantitative predictions for self-writing do not agree with self-writing observations in planar germanosilicate glass. To obtain good agreement with these observations, an exposure-dependent loss must be included (see Section 5.3 and Ref. [28]). We assume here that the loss evolves in the same way as the index, and the total loss can thus be written as

$$\alpha = \alpha_0 + \gamma k_0 \Delta n, \tag{10}$$

where α_0 represents the constant loss and γ is a proportionality factor. Equation (10) is the simplest model relating loss and index changes, and also follows from basic Kramers-Kronig arguments and the assumption that a common mechanism underlies these changes. This model for the light-induced change to the material loss is considered in Section 5.3. All discussions before then assume no loss or a constant loss.

In addition to refractive index changes and loss, many photosensitive materials also exhibit luminescence which we discuss later as a characterisation tool. Like the index and the loss, the strength of the luminescence can undergo cumulative light-induced changes as well. We do not develop any quantitative models of this process but do refer to it briefly in Section 5.4.

2.3.3 A phenomenological description of photosensitivity

Here a simple phenomenological model is used for photosensitivity. We assume that the refractive index increases in response to illumination. Observations in Section 5 are consistent with index increases, and so it is sufficient to model index increases here.

The one-photon model in Eq. (9) is used to describe photosensitivity at 244 nm. At 488 nm, Eq. (8) is used, as in Refs [21] and [22]. Although these models serve well when the index changes are small, it is sometimes necessary to incorporate saturation effects. The index change saturates to Δn_s, and the

increase in Δn slows exponentially as Δn_s is approached. This model has been used for saturation in a photopolymer [29], and it agrees with the experiments at 488 nm by Hand *et al.* [20]. Hence the evolution of the refractive index is described using

$$\frac{\partial \Delta n}{\partial t} = A_p (\mathcal{E}\mathcal{E}^*)^p \left(1 - \frac{\Delta n}{\Delta n_s}\right). \tag{11}$$

For a one-photon photosensitivity process, $p = 1$, and for a two-photon process $p = 2$. The real coefficient $A_p > 0$ depends on p, the material properties and the wavelength of the writing beam.

2.4 The model in dimensionless form

Self-writing can be described using Eqs (5) and (11) along with an incident beam profile. A Gaussian writing beam with width a is often used [Eqs (6)]. Hence, including the two parameters associated with the initial condition, there are five free parameters ($\mathcal{E}_0$, a, α, A_p and Δn_s). The number of independent variables can be reduced using dimensionless variables. The length scale depends on the beam width, and the time scale depends on the intensity, so we define $X = x/a$, $Y = y/a$ and $E = \mathcal{E}/\mathcal{E}_0$. Using the dimensionless variables:

$$Z = z/(k_0 n_0 a^2) \tag{12a}$$
$$N = a^2 k_0^2 n_0 \Delta n \tag{12b}$$
$$N_s = a^2 k_0^2 n_0 \Delta n_s \tag{12c}$$
$$T = a^2 k_0^2 n_0 A_p (\mathcal{E}_0 \mathcal{E}_0^*)^p t \tag{12d}$$
$$L = a^2 k_0 n_0 \alpha = a^2 k_0^2 n_0 \gamma \Delta n \tag{12e}$$

Eqs (5) and (11) become

$$i\frac{\partial E}{\partial Z} + \frac{1}{2}\nabla^2 E + NE + \frac{iL}{2}E = 0 \tag{13}$$

and

$$\frac{\partial N}{\partial T} = (EE^*)^p \ (1 - N/N_s) \tag{14}$$

where $\nabla^2 = \frac{\partial^2}{\partial Y^2}$ for the planar geometry, or $\nabla^2 = \frac{\partial^2}{\partial X^2} + \frac{\partial^2}{\partial Y^2}$ in bulk. The input profile becomes

$$E(Y,0,T) = \exp\left(-Y^2\right) \quad or \quad E(X,Y,0,T) = \exp\left(-X^2 - Y^2\right), \tag{15}$$

and the Rayleigh range is $Z_R = 1/2$.

Using these coordinates, the system formed by Eqs (13), (14) and Eq. (15) does not depend on a, A_p or $\mathcal{E}_0$, and the remaining parameters are N_s and L. This simplification makes the problem more tractable: more generally, for any incident beam that can be described by two parameters, the parameter space is reduced from five to two dimensions. If, in addition, both loss and saturation can be ignored, there is only one problem to be solved, and this is approximately valid in a wide variety of circumstances. In general, the system can always be reformulated to remove 3 parameters.

3 Phenomenology of self-writing

Section 3.1 describes a numerical simulation technique which can be used to explore the evolution of a self-written waveguide, and in Section 3.2 some results for the planar two-photon process are presented. These are the results which are most directly relevant to the experiment in Section 5. Although ultimately a channel forms, the details of this evolution are surprisingly complex. The results for the one-photon process are similar in many respects, and are presented in Section 3.3 and Refs [24, 30]. In this section material loss is ignored; the effects of losses are discussed in Section 5.

3.1 Numerical simulations

Self-writing is described by two partial differential equations [Eqs (13) and (14)], along with an initial condition for the incident beam. The most straightforward way to solve this system is using a numerical split-step method [17, 31] on a grid within the material. This simulation is an important benchmark against which the other results can be compared. Results of this numerical simulation technique as applied to the self-writing process are given in Refs [30, 24, 32].

Two distinct processes comprise self-writing; the propagation of light, and the evolution of the refractive index distribution. The first process occurs on the time-scale of nanoseconds, whereas the second takes minutes (see Section 1.2). The simulation described here takes advantage of this difference in time-scales to separate these processes into two independent steps. Thus we first allow light to propagate through the structure. Then we update the refractive index distribution to account for the photosensitive refractive index change due to this light distribution. Light is then propagated through this altered refractive index structure, and so on. Our implementation is accurate to second order in both the temporal step size and spatial step size in the propagation direction.

3.2 Two-photon results

3.2.1 Overview for $p = 2$

Here a selection of contour plots detail how a self-written waveguide evolves when $p = 2$ and the writing beam is taken to be Gaussian. Fig. 3 shows intensity contour plots, and Fig. 4 shows the corresponding refractive index plots.

The beam is incident from the left, and the material is viewed from above. The horizontal axis is the propagation direction (Z), the vertical axis is the transverse direction (Y). Although the contour levels are equally spaced, the absolute levels vary between figures. Only the region of interest around the propagation axis is shown; *i.e.* the transverse distance shown in the plots is significantly less than that used in the calculations. The propagation distance is $Z = 2$, corresponding to 4 Rayleigh ranges; this is equivalent to a distance of about 2 mm when a 8 μm writing beam at 488 nm is used, as in Section 5 [see Eq. (12a)].

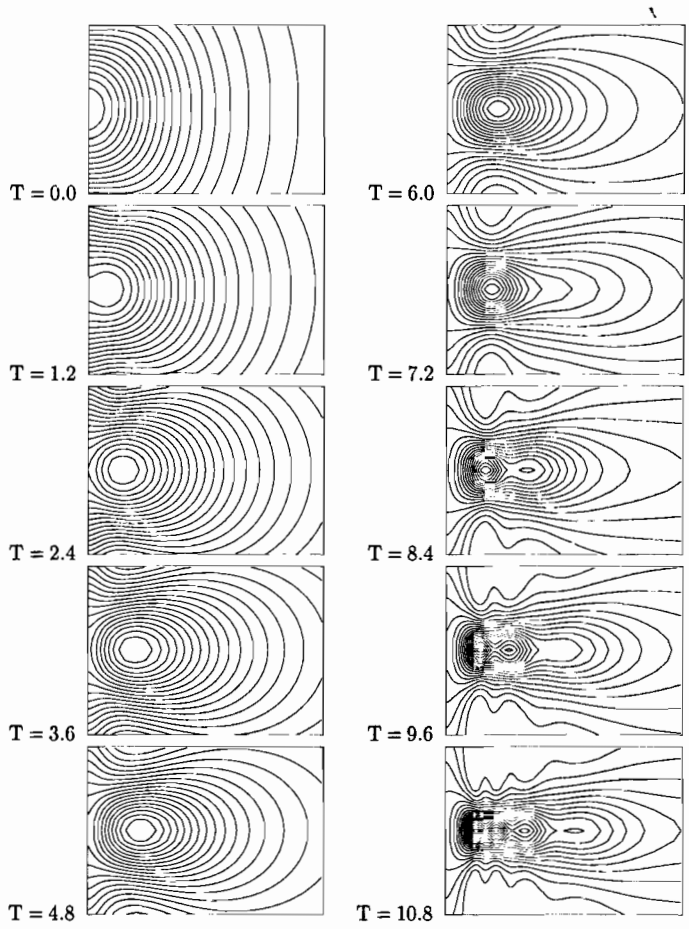

Figure 3: Intensity contours for $p = 2$.

As Fig. 3 shows that over time the beam becomes guided along the propagation axis by the refractive index change it induces in the material. The contour plots show that a number of maxima form in the intensity distribution during this process, and they are described in detail in Section 3.2.2. The first contour plot in Fig. 4 is blank because the refractive index is initially uniform in the plane. A maximum also forms in the index distribution. Over time the index distribution beyond this maximum evolves into a channel waveguide.

3.2.2 Details of the evolution for $p = 2$

When the beam is switched on it diffracts freely, and, as can be seen in the first frame in Fig. 3, the intensity is highest at the origin. The index increases most rapidly in regions of high intensity [see Eq. (14)], and so it initially increases most at the origin. The incoming beam then passes through this region, which

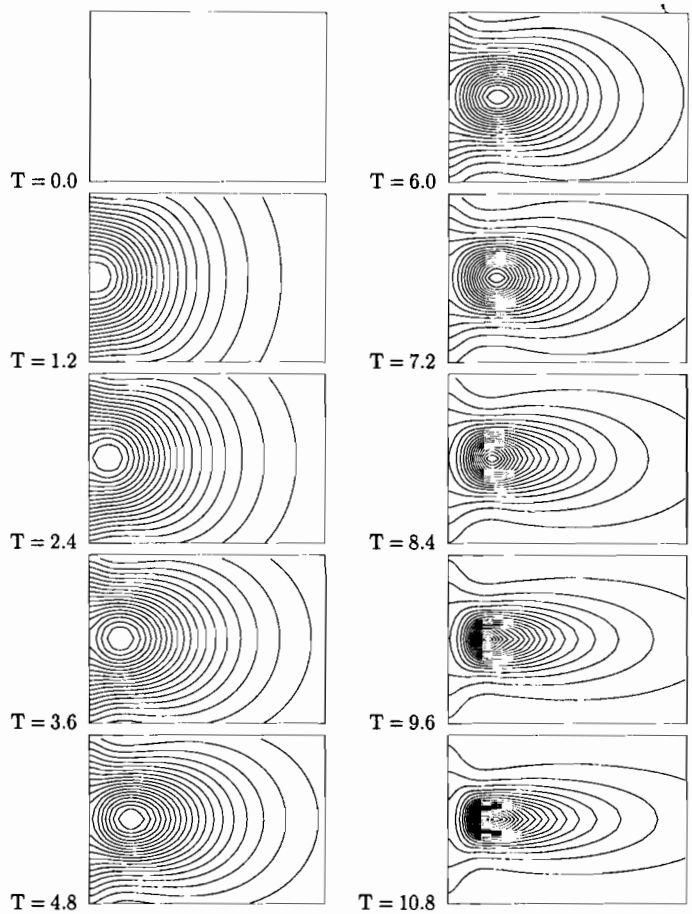

Figure 4: Refractive index contours for $p = 2$.

reduces its diffraction.

For times $T < 0.5$, the intensity at $y = 0$ decreases monotonically with Z. However, at $T = T_0 = 0.5$, the intensity forms an inflection point at $Y = 0$, $Z = 0$. For $T > T_0$, this point evolves into a minimum at the origin and a maximum that moves out along the propagation axis over time. We refer to this maximum as the *primary eye*. This feature is a landmark in the self-writing process; it forms because light is focussed by the increased refractive index near the input face. Hence at this time, diffraction has to some extent been overcome by the index change. In Section 4.1, exact expressions for T_0 (the eye formation time) are found for a variety of situations. For future reference this formation time is labelled $T_0^{(2)}$ for $p = 2$, or $T_0^{(1)}$ for $p = 1$. As Fig. 3 shows, the primary eye moves along the propagation axis as self-writing proceeds. At time $T \approx 5$, the eye turns around and moves back towards the input face. This movement

is indicated by the solid line in Fig 5.

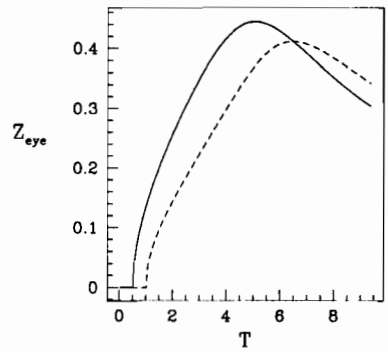

Figure 5: Solid line: position of the intensity primary eye on the propagation axis versus time for $p = 2$; Dashed line: position of the refractive index eye.

A similar primary eye also forms in the index distribution at $T = 2T_0^{(2)} = 1$, as can be seen in Fig. 4. This eye forms due to the accumulated intensity near the input face caused by the intensity eye, which explains why the index eye forms later. After it forms, the refractive index eye moves in similar manner to the intensity eye (dashed line in Fig. 5). The eyes are merely local maxima, and not physical objects, and so their movement does not imply that energy is transported.

As time progresses, additional maxima form on the propagation axis in the intensity distribution, and these are referred to as *secondary eyes.* The first secondary eye forms on the right edge of the primary eye and moves to the left towards the primary eye. The second secondary eye forms on the trailing right edge of the first secondary eye, and so on. This can be seen most easily by looking at intensity cross-sections taken along the propagation axis. Note that the leftmost maximum is always the primary eye. The left half of Fig. 6 shows the axial intensity at $T = 8.5$. At this time one secondary eye has formed on the right edge of the primary eye. By $T = 9.5$, this first secondary eye has moved to the left, towards the primary eye, and a second secondary eye is forming to the right of the first one, and this pattern continues over time.

As the self-written channel evolves, it becomes deeper with time. At some stage in the evolution, it becomes deep enough to support two even modes, which can then beat; the beat pattern is observed is secondary eyes. The secondary eyes move sufficiently fast that their effect on the refractive index distribution is smeared out. Note from Fig. 3 that the secondary eyes are not equally spaced along the propagation axis. By $T = 10$, most of the light is confined transversely for some distance in the slab. Beyond the primary eye region, the refractive index has evolved into a fairly uniform self-written channel waveguide.

After the refractive index primary eye has formed, these simulations show that it is always the point of highest refractive index change in the material. At $T = 12$, the dimensionless index change at the eye is $N \approx 84$. Using Eq. (12b),

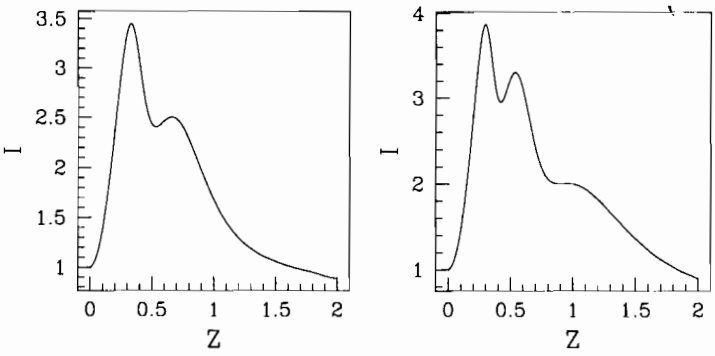

Figure 6: On-axis intensity for $p = 2$ at $T = 8.5$ (left) and $T = 9.5$ (right).

this corresponds to $\Delta n \approx 7 \times 10^{-3}$ at 488 nm when we take $n_0 = 1.492$ and an intensity FWHM of 8 μm, as in Section 5. This is larger than the refractive index changes typically achieved in these materials, and so saturation is important in the later stages of the evolution ($T \gtrsim 10$).

3.3 One-photon results

Here results for the one-photon photosensitivity process in the planar geometry are presented, and again a Gaussian beam is used.

3.3.1 Overview for $p = 1$

Fig. 7 shows how the intensity evolves for $p = 1$, and Fig. 8 shows the corresponding index plots. Although the same features form as for $p = 2$, there are a number of qualitative differences, as discussed below.

3.3.2 Details of the evolution for $p = 1$

Initially, the beam diffracts freely, and so the one and two-photon processes are indistinguishable. As for the two-photon process, there is a time T_0 at which an inflection point forms in the intensity on the propagation axis. For a Gaussian input beam, $T_0^{(1)} = 1$ where the superscript denotes $p = 1$. Note that the times for the one and two-photon processes do not correspond, as the material constants differ. As for the two-photon case, a primary eye also forms in the refractive index, and again this occurs at time $T = 2T_0^{(1)}$. Figs 7 and 8 show that these eyes move in a similar manner as for $p = 2$.

The first qualitative difference between the one and two-photon processes becomes evident when the secondary eyes begin to form. Fig. 7 shows that for $p = 1$ the secondary eyes move along the propagation axis from large Z towards the input face. Recall that for $p = 2$, the secondary eyes form on the right edge of the primary eye. As mentioned, these eyes form due to the beating of the first two even modes of the evolving waveguide, and the difference in their motion

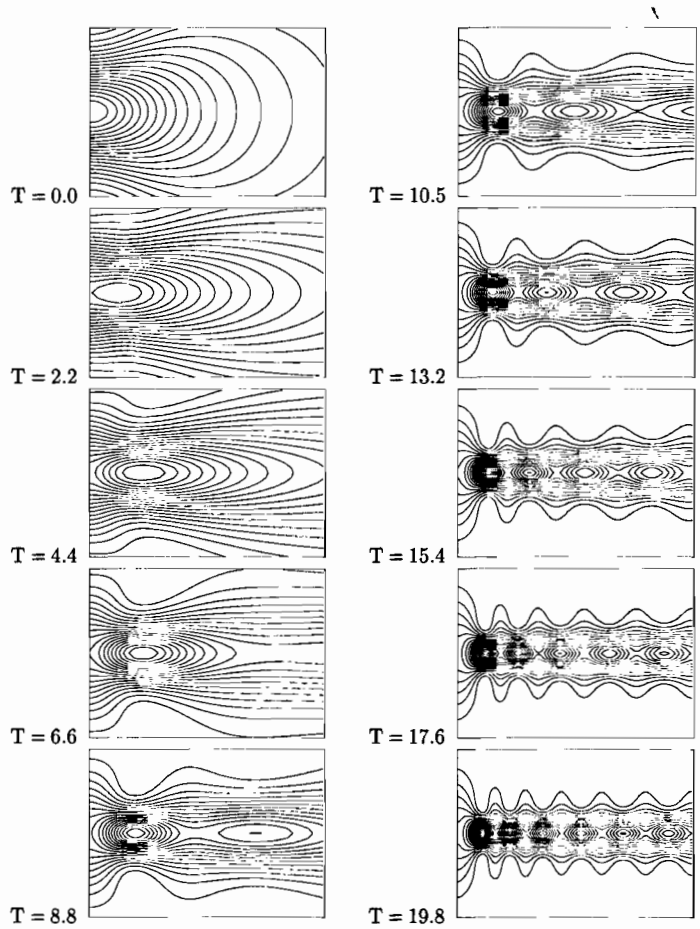

Figure 7: Intensity contours for $p = 1$.

can be understood using WKB analysis (see Section 3.4 [24]). As the secondary eyes continue to form, they remain much more evenly spaced for $p = 1$ than for $p = 2$ (see Fig. 7). Also notice that the channel waveguide which ultimately forms in Fig. 8 is noticeably more uniform than the $p = 2$ waveguide shown in Fig. 4.

The maximum dimensionless refractive index change in the material at $T = 22$ is $N \approx 45$. Using Eq. (12b), this corresponds to $\Delta n \approx 10^{-3}$ at 244 nm when we again take $n_0 = 1.492$ and an initial intensity FWHM of $8\,\mu$m, as in the experiment in Section 5. Refractive index changes of this magnitude are achievable in this HCPECVD material [9], and so it is justified to ignore saturation here. Although at some stage saturation must begin to play a role, the time at which this occurs is much later than for $p = 2$.

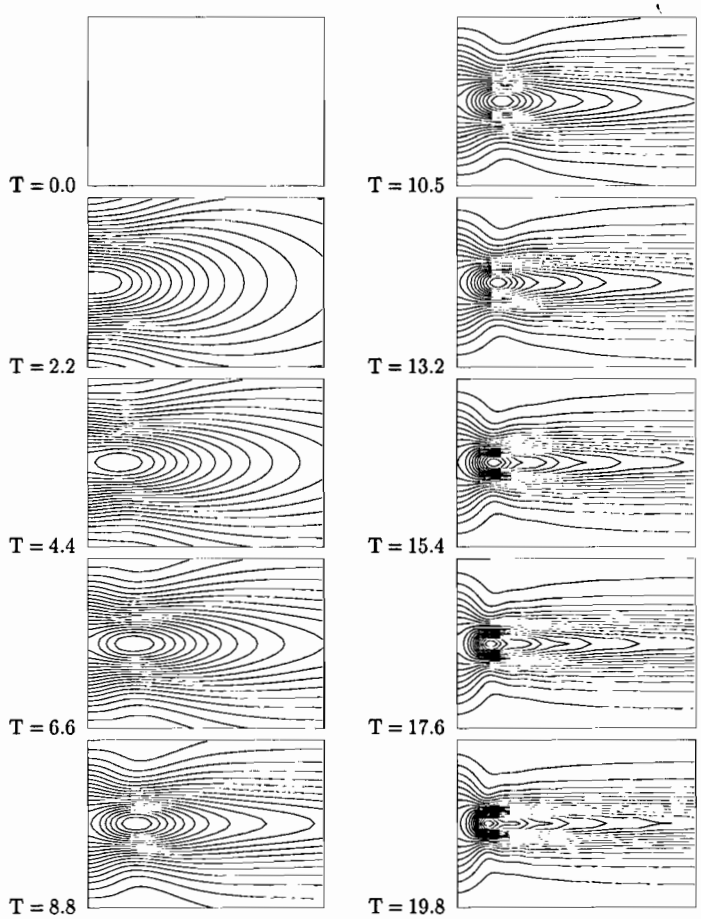

Figure 8: Refractive index contours for $p = 1$.

3.4 WKB analysis

WKB analysis provides insight into the modal properties of self-written waveguides [24], and this approach can be used here because the transverse structure varies smoothly. At early times in the self-written evolution, the index change is approximately determined by the initial intensity profile [see Eq. (14)]. We have shown that therefore for $p = 2$ at early times the number of modes supported is constant throughout the slab, and the structure then thus acts as an efficient mode converter.

WKB analysis confirms the finding that for the $p = 2$ case the secondary eyes form just to the right of the primary eye, as described in Section 3.2. WKB analysis also predicts that the distance between the secondary eyes varies with propagation distance, as can be seen in the contour plots in Fig. 3, and indeed the quantitative predictions for the distances between the eyes are in

close agreement. These results have been described in detail [24], along with results of the WKB analysis for $p = 1$. In this case, WKB analysis corroborates the fact that the secondary eyes move towards the input face from the right. It also predicts that the distance between the secondary eyes is roughly constant.

Secondary eyes always form during the formation of a channel waveguide, and here it has been shown that they form as a result of mode beating. Hence, by definition, at the writing wavelength the waveguide is multimoded. However, once the waveguide has been written, it can guide light at other wavelengths, and it may then be single moded.

3.5 Simulation results for the bulk geometry

Even though self-writing has been observed in a range of bulk materials [1, 32, 29] (see Section 6), no bulk numerical simulations have previously been reported. While the implementation of the numerical simulation technique is no more complicated for the bulk geometry than for the planar geometry, it requires significantly more computational resources. The bulk calculation is well suited to a vectorized supercomputer, as many of the calculations are independent.

Although saturation can often be ignored in the planar geometry, this cannot be done in the bulk geometry. If saturation is ignored, the refractive index change at the primary eye grows prohibitively large before a channel can form at larger Z. One way of understanding this difference is to consider the initial build up of refractive index near the input face in terms of a lens. The primary eye is the point at which the beam is focused to a waist by this lens. For the bulk case, the incoming light is focussed to a waist in both transverse dimensions. In contrast, in the planar case, the lens only focuses one transverse dimension. Hence the intensity at the waist is much higher for the bulk geometry, which leads to a much more rapid change in index at the primary eye [see Eq. (14)], and hence the effect of saturation needs to be considered much earlier. An analogous effect is observed with spatial solitons based on the Kerr effect; although in two dimensions they are stable, in three dimensions they collapse [33]. Here we halt this collapse by introducing saturation in our model.

3.5.1 Results for a circularly-symmetric input beam

Here the results from a typical bulk calculation are presented. The input beam is again taken to be a Gaussian of the form in Eq. (15). As this beam is circularly-symmetric, it suffices to show slices through one of the transverse axes. The refractive index change is taken to be a one-photon process, as this is the case which corresponds to the bulk photopolymer experiments of Kewitsch and Yariv [32, 29] (see Section 6.2). We take the dimensionless saturation index to be $N_s = 160$ (see Section 3.5.2 for discussion of the choice of N_s).

Initially, light diffracts freely throughout the material, and at $T \approx 1$, an inflection point forms in the intensity. Again, this point becomes a primary eye, which moves away from the input face, and a minimum at the input face. Note that the inflection point does not form exactly at $T = 1$ as it does for the

planar $p = 1$ case, but slightly later. The eye moves away from the input face after it forms, and this movement is quantitatively similar to the planar case (see Fig. 5). A primary eye also forms in the index distribution.

The secondary eyes form in the same way as in the planar geometry; for the $p = 1$ case, they move towards the input face from the right. Fig. 9 shows the contours at time $T = 15$, when six secondary eyes are present. Observe that the secondary eyes are not spaced as evenly as in the corresponding planar case. At this time, a channel has evolved in the material. The maximum $N = 105$ in Fig. 9 approaches the saturation value $N_s = 160$ used here, and so saturation is significant by this stage in the evolution.

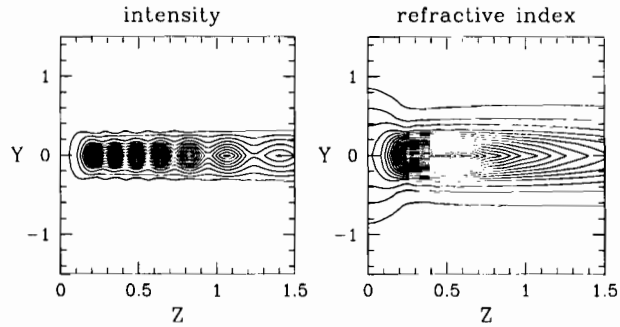

Figure 9: The intensity and refractive index in a bulk material at $T = 15$, $X = 0$.

3.5.2 Effect of saturation

The results in Section 3.5.1 were calculated using the saturation value $N_s = 160$, corresponding to $\Delta n_s \approx 4 \times 10^{-3}$ for a $10\,\mu$m beam at 325 nm, which is readily achievable in photopolymers [32]. These results indicate that the bulk self-written evolution for $N_s = 160$ closely resembles the planar results. This similarity diminishes as N_s is reduced, which is not surprising, as the planar results were calculated with $N_s = \infty$. In photosensitive glass the obvious choice of writing wavelength is 488 nm (see Section 5). At this wavelength, if the incident beam width is $10\,\mu$m, $N_s = 160$ corresponds to $\Delta n \approx 9 \times 10^{-3}$ [see Eq. (12c)], which is typically not possible in glass. Here we review how self-writing is affected when N_s is lowered. As self-writing in bulk photosensitive glass has not yet been observed, this study has important experimental implications.

Recall from Section 3.3 that for the planar geometry, where $N_s = \infty$, the intensity primary eye forms at $T_0 = 1$. As N_s is reduced, T_0 increases; *i.e.* the eye forms later in a material with a lower saturated index. Indeed, as N_s is reduced, the most obvious effect is that self-writing proceeds more slowly, which is not surprising [see Eq. (14)]. A more subtle change occurs to the motion of the eyes as the effect of saturation is increased. Fig. 10 shows the eye position over time when $N_s = 10$. At 488 nm, a $10\,\mu$m incident beam, $N_s = 10$ corresponds to $\Delta n_s \approx 6 \times 10^{-4}$, lower than the saturation value in most photosensitive glasses.

At $T \approx 18$, the eye begins to move back away from the input face, and so the behaviour differs qualitatively for small saturation values.

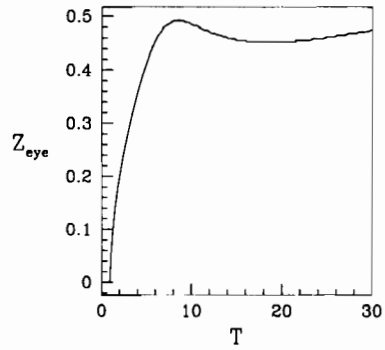

Figure 10: Position of the intensity primary eye for the bulk geometry when $N_s = 10$. The eye motion changes qualitatively when N_s is small (*c.f.* Fig. 5).

If $N_s \lesssim 15$, then the eye movement has the form shown in Fig. 10. This is undesirable, because if the eye is located at large Z, the channel-like region must begin at even larger Z. Using a $10\,\mu$m writing beam at 488 nm, $N_s = 15$ corresponds to $\Delta n_s \approx 8 \times 10^{-4}$. Hence to avoid this, we require the material to have $\Delta n_s \gtrsim 8 \times 10^{-4}$. This is an important constraint, because photosensitive glasses can have a saturation index near this value. Note however that if a material has a lower saturation value, this undesirable effect can still be avoided by using a slightly wider input beam. Doing this reduces the Δn_s that corresponds to $N_s = 15$ [see Eq. (12c)]. However, by Eq. (7), a wider beam requires a longer sample, and so this effect, in effect, sets a lower bound for N_s.

4 Theoretical investigations

4.1 Exploration of the primary eye

As described in Chapter 3.1, when the waist of a Gaussian beam is focused at the input face, the intensity is highest there. After some time, the refractive index change built up in this region becomes large enough to counteract the diffraction of the beam, and this point of maximum intensity moves away from the input face. The time at which this occurs is labelled $T_0 = T_0^{(1)}$ for $p = 1$ or $T_0 = T_0^{(2)}$ for $p = 2$. For $T > T_0$, this maximum is referred to as the *primary eye*, and so we refer to T_0 as the time at which this eye forms. A similar maximum also forms in the refractive index distribution at a later time, and the locations of these maxima change over time. Ultimately a channel waveguide is formed in the region beyond the primary eye in the refractive index distribution.

Our numerical results described in Sections 3.2 and 3.3, suggest that the eye is always a precursor to the formation of a waveguide. For complicated

beam shapes, we find that primary eyes typically form at the maxima in the transverse intensity profile. Furthermore, simulations indicate that the structure of the resulting waveguide is closely related to the trajectories of eyes within the material.

Gaussian optics can be used to gain some understanding of the primary eye dynamics; the refractive index that builds up behind the input face acts like a gradient index lens on the incident beam. After some finite time, the strength of this lens increases to the point when it can focus the incoming beam to a waist (the primary eye). As time passes, the index at the input face increases. Hence the lens strength $(1/f)$ also increases with T, where f is the dimensionless focal length [34]. If the Gaussian beam in Eq. (15) were focused by a thin lens at the origin, the image position would be [16] $i = f/(1+f^2)$. A plot of i versus the lens strength $(1/f)$ produces a curve that is qualitatively the same as Fig. 5. Hence Gaussian optics explains why the eye initially moves away from the origin, then at a later time turns around and moves back.

Next we describe an analytical series expansion technique that can help us to obtain a fuller understanding of the behaviour of the primary eyes, and the way in which their motion is linked to the form of the resulting waveguide. Although the following discussion refers to intensity eyes, the analysis is equally valid for index eyes, and the planar geometry is considered here for ease of notation. Also, we consider input beams for which there is initially no maximum present in the material.

By definition, the primary eye forms at time T_0, at position (Y_0, Z_0) in the material. As eyes are local maxima, both eigenvalues of the Hessian matrix

$$\mathcal{H} = \begin{pmatrix} \frac{\partial^2 I}{\partial Z^2} & \frac{\partial^2 I}{\partial Z \partial Y} \\ \frac{\partial^2 I}{\partial Z \partial Y} & \frac{\partial^2 I}{\partial Y^2} \end{pmatrix} \tag{16}$$

must be negative at the eye position, where $I = I(Y, Z, T)$ is the intensity. This leads to the requirement that

$$\mathrm{Det}(\mathcal{H})|_{(Y_0, Z_0, T_0)} = 0 \tag{17}$$

when an eye forms. After the eye forms, it remains a local maximum, and so at the eye position

$$\frac{\partial I}{\partial Z} = 0 \quad \text{and} \quad \frac{\partial I}{\partial Y} = 0. \tag{18}$$

Eqs (17) and (18) are a prescription for finding the time and position at which the eye forms (T_0, Z_0). Eqs (18) can also be used to find the trajectory of the eye after it forms.

The numerical simulations in Section 3.1 show that when a Gaussian writing beam is used, the primary eyes are typically located near the input face. To illustrate this, note that for the planar two-photon process, Fig. 5 shows that the maximum distance of the eye from the input face is $Z \approx 0.44$, a distance of less than one Rayleigh range. Also, note that the eye is located at very small Z for early times. This suggests that Taylor series expansions for the intensity

and the refractive index in Z about the input face ($Z = 0$) may provide useful information about the eyes. Section 4.1.1 describes the way in which these series expansions are calculated.

4.1.1 Calculation of the series expansions

The writing beam is taken to be the arbitrary function $E_0(Y)$ for the planar case, or $E_0(X,Y)$ for bulk. The dimensionless electric field amplitude and refractive index are written as the following Taylor series expansions

$$E = \sum_{q=0}^{\infty} E_q Z^q \quad \text{and} \quad N = \sum_{q=0}^{\infty} N_q Z^q. \tag{19}$$

As in Section 2, the normalized intensity is defined to be $I = EE^*$, which is

$$I = \sum_{q=0}^{\infty} I_q Z^q, \quad \text{and so} \quad I_q = \sum_{k=0}^{q} E_k E_{q-k}^*. \tag{20}$$

The coefficients E_q, I_q and N_q depend on T and Y in planar geometries, and on T, X and Y in bulk; these dependencies are kept exact throughout the analysis.

A recurrence relation for the electric field coefficients can be found by using Eqs (19) in Eq. (13) and equating coefficients of Z^{q-1}:

$$E_q = \frac{i}{q}\left(\frac{1}{2}\nabla^2 E_{q-1} + \sum_{k=0}^{q-1} N_k E_{q-1-k} + \frac{iL}{2} E_{q-1}\right). \tag{21}$$

Similarly, the photosensitivity equation [Eq. (14)] can be used to find a recurrence relation for the index coefficients (N_q). For the one-photon process

$$\frac{\partial N_q}{\partial T} + \frac{I_0}{N_s} N_q = I_q - \frac{1}{N_s} \sum_{k=0}^{q-1} N_k I_{q-k}. \tag{22}$$

Integrating Eq. (22) gives the following recurrence relation for the refractive index coefficients for the one-photon process

$$N_q(T) = \int_0^T \frac{I_q(T')}{Q(T'-T)} dT' - \frac{1}{N_s} \sum_{k=0}^{q-1} \int_0^T \frac{N_k(T') I_{q-k}(T')}{Q(T'-T)} dT', \tag{23}$$

where $Q(T)$ is defined to be

$$Q(T) = \exp\left(-I_0{}^p T / N_s\right). \tag{24}$$

For the two-photon process, again using Eqs (19) and (20) in Eq. (14), equating coefficients of Z^q and separating out the N_q terms gives

$$\frac{\partial N_q}{\partial T} + \frac{I_0^2}{N_s} N_q = \sum_{\ell=0}^{q} I_\ell I_{q-\ell} - \frac{1}{N_s} \sum_{k=0}^{q-1} \sum_{\ell=0}^{q-k} N_k I_\ell I_{q-k-\ell}. \tag{25}$$

Integrating Eq. (25) gives the following recurrence relation for $p = 2$

$$N_q(T) = \sum_{\ell=0}^{q} \int_0^T \frac{I_\ell(T') I_{q-\ell}(T')}{Q(T'-T)} dT' - \frac{1}{N_s} \sum_{k=0}^{q-1} \sum_{\ell=0}^{q-k} \int_0^T \frac{N_k(T') I_\ell(T') I_{q-k-\ell}(T')}{Q(T'-T)} dT'. \quad (26)$$

The time dependencies are shown explicitly in Eqs (23) and (26), whilst the dependencies on the spatial coordinates are suppressed.

Starting with the incident beam profile (E_0), Eqs (21) and (23) or (26) can be used to generate the terms in the field and index expansions. The terms in these expansions rapidly become quite complicated for the general case. However, if saturation is ignored ($N_s \to \infty$, so that $Q = 1$), then the integrals can be performed in closed form for every term, and the results then simplify considerably [30]. All results presented here are based on Taylor series expansions in the propagation distance Z. If Z_c is the radius of convergence of the expansion, then the expansions only yield physically relevant information for $Z < Z_c$. The expansions provide useful information about the primary eyes because these eyes are often located at small Z. In Section 4.1.3 the reason for the limited region of validity of these series expansions is discussed.

Application of the series technique to Gaussian beams

This section reviews the results of the series expansion technique for a Gaussian input profile in a planar material. This simple input profile allows significant progress to be made with this method. Loss and saturation are ignored, for simplicity, although they are considered in later sections. For the examples given here $p = 2$ is chosen to relate to the experiments described in Section 5. To $O(Z^4)$, the intensity expansion on the propagation axis is

$$I = 1 + (4T - 2)Z^2 + \left(6 - 152T + \frac{80T^2}{3}\right) Z^4 + O(Z^6). \quad (27)$$

At $T = 0$, to $O(Z^2)$ Eq. (27) is a decreasing function of Z, as expected, since at this time the beam diffracts. Eq. (27) predicts that at $T = 0.5$, the Z^2 term vanishes, and for $T > 0.5$ the intensity increases with Z. Far from the input face, I must decrease with Z, as the beam eventually begins to diffract again. Therefore, when $T > 0.5$, there must be an intensity maximum somewhere on the propagation axis. Hence the series expansion predicts that the primary eye forms at $T_0^{(2)} = 0.5$, consistent with the result found in Section 3.2.

Using terms to order Z^4 in Eq. (27), the location of the intensity eye shortly after it forms can be found. This is done by solving Eq. (18), and expanding the solution about the formation time $T_0^{(2)}$. To lowest order the eye location at early times after its formation is given by

$$Z_{eye} = \sqrt{\frac{3}{95}\left(T - T_0^{(2)}\right)}. \quad (28)$$

Eq. (28) gives excellent agreement with the numerical simulations for early times after the eye formation. Regardless of the number of terms used, the agreement breaks down at $Z \approx 0.25$, $T \approx 2$. This suggests that at this time, the radius of convergence of the series is $Z_c \approx 0.25$. Using terms up to $O(Z^8)$ allows us to capture the movement of the primary eye back towards the input face at later times. For $5.8 < T < 26$ we find that to this order the expansion has no maximum, and so clearly for these times the eye is outside the radius of convergence. It might seem surprising that we can capture the primary eye at late times after losing it earlier. However recall that this is an initial value problem; the properties of the waveguide at Z' can only depend on the previous history of the waveguide for $Z \leq Z'$.

The behaviour of the primary eye in the refractive index can also be explored using the series technique, and the agreement with the simulation results is similarly good. The same is true for the one-photon case, although these results are not shown here for brevity.

Results for an arbitrary beam

Some quite general and exact results can be obtained for the eye trajectories if the series expansions only contain even powers of Z. The first odd term in the intensity expansion is

$$I_1 = \mathrm{Im}\left(E_0^* \nabla^2(E_0)\right) - LI_0. \tag{29}$$

It is possible to show that I_1 vanishes for all values of the transverse coordinate(s), only if $L = 0$, and if the beam also has a flat phase front. Under this condition, all other odd terms vanish as well.

Here for simplicity we consider a flat phase-front beam in a lossless planar geometry. Recall from Sections 3.2 and 3.3 that in a planar geometry, we can neglect saturation early in the evolution *i.e.* take $N_s = \infty$. Using the series expansion to order Z^2, we find that an intensity primary eye forms at time T_0 defined via

$$4pE_0^{2p}T_0 = \frac{E_0''}{E_0} - \frac{E_0''''}{E_0''}. \tag{30}$$

where primes denote derivatives with respect to Y evaluated at Y_0. The right-hand side of Eq. (30) does not depend on the refractive index evolution and is a measure of how strongly the beam diffracts at small Z. The fourth derivative indicates that the initial diffraction is very sensitive to the beam profile. The left-hand side of Eq. (30) is proportional to the index change at the input face. The refractive index change in the input face region acts like a lens on the incident beam, and the left side of Eq. (30) is a measure of the strength of this lens. At T_0, the lens has grown strong enough to counteract the diffraction of the beam, and focuses the incoming beam into a waist, forming an eye.

Trajectory of the primary eye

We can now calculate the initial trajectory of the intensity eye after it has formed for the planar geometry with an arbitrary shaped writing beam. Most

primary eyes form at $Z = 0$, and we consider only this case here. Expanding the intensity about the eye formation point and using Eq. (18) leads to the finding that regardless of the input beam shape, the primary eye in the intensity always initially moves away from the input face in a parabolic trajectory. This occurs for both one and two-photon processes. The Gaussian beam is a degenerate example: the trajectory is a straight line.

The same analysis can be performed for the refractive index eye. We find the unexpected result that to lowest order the index eye always moves along the same parabolic trajectory as the intensity eye, although at a different rate. This is true for both one and two-photon photosensitivity processes. More generally, when loss is included, the intensity and index eyes still initially follow the same trajectory. Simulation results show that the eye trajectories remain similar for a remarkably long time. This is surprising, because the refractive index at time T depends on the entire history of the illumination. Hence we can make predictions about the resulting waveguide using only the intensity expansion. This is particularly useful, as the terms in the refractive index expansion take longer to calculate and are often more complex than the corresponding terms in the intensity expansions.

4.1.2 Effect of material properties on self-writing

As all materials exhibit loss and saturation effects, we present here a series expansion analysis of how these affect the self-writing process.

Effect of loss

We consider here the effect of loss in the planar geometry for the two-photon photosensitivity process. This choice is made to correspond to the experiments in Section 5. Loss can cause a quite profound change to the self-written evolution, and in particular, if the loss is too high, it impedes the formation of a self-written waveguide. The results for the one-photon case are very similar to the two-photon results, and so are not shown here for brevity. We expect that the effect of loss should be similar in a bulk material.

For simplicity, we again take the input beam to be Gaussian. There are odd terms in the series expansions for a lossy material because to lowest order, loss causes the intensity to drop off linearly with distance into the material. Hence if a primary eye forms in a lossy material, it cannot form at the origin, and must form a finite distance into the sample, at some position Z_0. We treat the loss (L) as a small parameter here in order to make this problem tractable, since if L is small, then Z_0 is also small. When the loss is small, we can also treat $(T - T_0^{(2)})$ as a small parameter for a short time after the eye forms. Neglecting small terms in the intensity expansion, and using Eqs (17) and (18), we find that the eye forms at time

$$T_0^{(2)} \approx \frac{1}{2} + \frac{\sqrt[3]{95}}{4}\left(\frac{3L}{2}\right)^{2/3}. \tag{31}$$

Hence as expected, loss increases the time taken for the intensity eye to form. The eye forms on the propagation axis at position

$$Z_0 \approx \sqrt[3]{\frac{3L}{1520}}. \tag{32}$$

The fractional powers in Eqs (31) and (32) indicate that the presence of even a small amount of loss noticeably changes the dynamics of this process; the eye forms later, at a finite position within the slab.

Again using the intensity expansion, for small L, the position of the eye at time T just after it has formed is

$$T - T_0^{(2)} \approx \frac{190}{3}\left(Z^2 - 3Z_0^2 + 2\frac{Z_0^3}{Z}\right). \tag{33}$$

By examining Eq. (33) just after the eye forms at (Z_0, T_0), we observe that loss causes two stationary points to form at Z_0; a maximum and a minimum. After they have formed, the minimum moves towards the input face, while the maximum (the primary eye) moves away, as it did in the previous results. When $L = 0$, there is always a trivial minimum at the origin after the eye forms. Loss causes this minimum to form at a different position (Z_0), and to change its location over time.

Numerical simulations confirm the predictions (31) - (33). Fig. 5 shows the primary eye motion in the absence of loss, and Fig. 11 shows the associated series expansion result to $O(Z^4)$. A loss of 0.5 dB cm^{-1}, the value for the HCPECVD material used in Section 5, corresponds to $L \approx 0.01$. The movement of the maximum/minimum pair for $L = 0.01$ is shown in Fig. 11. It shows that at this loss level, the series prediction, although excellent, is not quite as good. This is because in these series results we assume that the loss is small, and hence as the loss is increased, the agreement with the simulation deteriorates.

For large values of loss, the minimum grows relatively deeper, and this has been demonstrated by both the series technique and the simulation. This minimum reduces the fraction of light guided along the central axis. If the loss is large enough, although an eye still forms, a channel waveguide does not form. This is at least partly due to the deepening of the minimum, which causes light to diffract away from the propagation axis. We have also investigated the effect of loss for $p = 1$, and find the same qualitative behaviour as for $p = 2$.

Effect of saturation

As shown in Section 3.5.2, in a bulk geometry, the saturation of the refractive index needs to be included to avoid the index growing without bound before a waveguide evolves in the material. Here we explore the effect of saturation when a Gaussian beam is incident on a bulk material. As in the numerical simulations in Section 3.5.2, we assume that the material is lossless for simplicity, and so there are no odd terms in the expansions. The examples shown here are for $p = 1$, because the bulk photopolymer experiments in Section 6.2 can be described using a one-photon model.

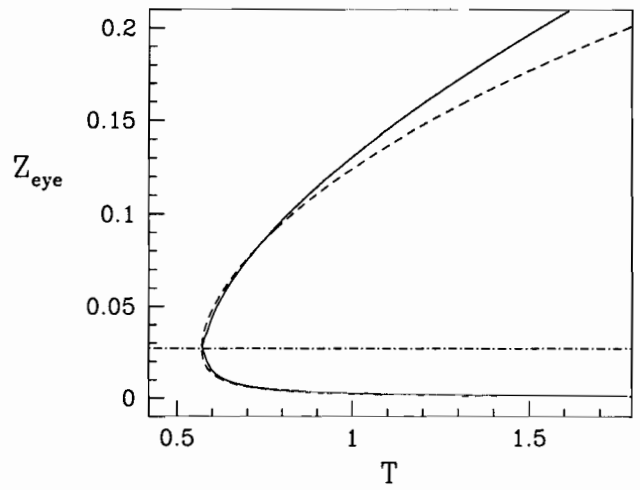

Figure 11: Dashed lines: positions of the maximum/minimum pair for 0.5 dB cm^{-1} for $p = 2$. The curve above the horizontal line corresponds to the eye, that below describes the minimum. Solid line: corresponding numerical simulation results.

The intensity primary eye forms at time T_0 which satisfies

$$pT_0 = \exp(T_0/N_s)\,. \tag{34}$$

If $N_s < e/p$, Eq. (34) can never be satisfied, and a primary eye cannot form. Eq. (12c) shows how N_s depends on the physical value of the saturation index (Δn_s), the diameter of the incident beam and the wavelength of the light. Hence in a given material, if the beam is too narrow, a waveguide cannot form. Conversely, for a given beam, if Δn_s is too small a waveguide cannot form. Eq. (34) predicts that T_0 increases as the saturation index is lowered, and so it takes longer to form a waveguide.

For small N_s (*i.e.* $N_s \lesssim 5$), the radius of convergence of the series decreases drastically. Hence for small N_s, even though we can predict whether an eye forms, the expansions do not provide useful information about the subsequent motion of the eye. This regime where N_s is small is unlikely to be of interest experimentally, because for typical beam diameters, this range of saturation values is substantially lower than found in real materials. For example, $N_s = 5$ corresponds to $\Delta n_s \approx 1 \times 10^{-5}$ for a 20 μm beam diameter at the one-photon wavelength of $\lambda = 244$ nm, significantly less than typical values of the saturation index ($\Delta n_s \approx 10^{-4} - 10^{-3}$, depending on the material). Hence for realistic saturation values the series expansions provide useful information.

Using the expansions to explore the motion of the eye, we find that the eye begins to move more quickly as the saturation value of the index is decreased from infinity. Note that $N_s = 15$ corresponds to $\Delta n = 1.3 \times 10^{-3}$ in the HCPECVD material described in Section 1.2, a reasonable saturation refractive index change in this material. For $N_s = 15$, saturation causes only about a 1%

change in the rate at which the eye moves away from the input face. Hence the value of the saturation index (N_s) is typically irrelevant at small times, and has little effect on the dynamics.

4.1.3 Generalizations of the series technique

Although the series technique is useful for describing the primary eyes while they are within the radius of convergence of the series, they typically move out of this region. It would be useful to extend the region of validity of the series to describe the entire motion of the primary eye. However, the obvious attempts to generalize this technique fail.

If the radius of convergence of a series is limited by a pole, Padé approximants can be used to remove the pole and hence extend the region of validity of the expansion [35]. We found that no good quantitative predictions for the eye motion could be obtained. The inability of this approach to give good results can be understood by considering the form of the electric field amplitude at $T = 0$. If the writing beam is a Gaussian in the planar waveguide geometry then on the propagation axis

$$E = (1 + 2iZ)^{-1/2}. \tag{35}$$

If Z is complex, then Eq. (35) has a branch point at $Z = i/2$, which restricts the range of Z for which the expansions are valid. It also limits the region of validity of any Padé approximant.

One established way of coping with singularities is to use the differential Padé generalization [36]. Then some differential combination of E is approximated by a generalized expansion Eq. (35) suggests the form

$$\frac{1}{E}\frac{\partial E}{\partial Z} = \frac{\sum_{s=0}^{M} A_s Z^s}{\sum_{t=0}^{N} B_t Z^t}. \tag{36}$$

However, it can be shown that for $p = 1$, even though Eq. (36) can be used to represent the field exactly at $T = 0$, an infinitesimal time ΔT later, the field contains singularities that cannot be expressed by Eq. (36). Thus even these Padé techniques cannot be used, and it is not clear how Eq. (36) should be generalized to account for these singularities. Although we cannot prove that the differential Padé generalization for $p = 2$ should fail, we find that the results given by this method are not significantly better than for $p = 1$.

4.1.4 Discussion

The series expansion technique is particularly useful for describing how material effects (e.g. saturation, loss and time delay in the material response) influence the self-written evolution. It can also be used to predict the structure of the waveguide written by any writing beam. However, unless the writing beam has a simple form, it is difficult to extract useful information from the series expansions.

4.2 Similarity results

Although useful for understanding the primary eye dynamics, the series expansion approch described in Section 4.1 cannot describe the subsequent formation of the channel waveguide. Here we use similarity techniques [37] to study this stage of the evolution, which leads to the first exact solution to the differential equations describing self-writing. We also show numerically that for a wide range of input beams, the self-written channel evolves toward this solution, which suggests that it is stable.

Similarity techniques have been used to study Hill-gratings [38], and to describe propagation in an inverted two-level medium [39]. Menyuk [40] used similarity methods to study stimulated Raman scattering, and he suggests that similarity techniques are generally useful for systems with a memory. Photosensitive glasses and photopolymers do exhibit such a memory.

Again we consider the planar geometry for simplicity. Because the structure evolves into a channel that is fairly uniform, we look for solutions where N is independent of Z. We also take the input beam $M(Y,T)$ to be a mode of this channel, and hence the field is of the form

$$E(Y,Z,T) = M(Y,T)\exp\left[i\beta(T)Z\right], \tag{37}$$

where β is the propagation constant, and M can be taken real. As the input beam is a mode, it changes as the waveguide evolves. We also choose to maintain constant input power:

$$\mathcal{P} = \int_{-\infty}^{\infty} M(Y,T)^2 dY. \tag{38}$$

Numerical results show that as the waveguide evolves, its shape remains approximately constant, even though its depth and width change [24]. Self-similar solutions depend only on certain combinations of the original variables, thus reducing the degrees of freedom of the system. We have found that the combination

$$\tilde{Y} = Y\phi(T) \tag{39}$$

is a universal parameter that can be interpreted as a time-dependent scaling of the transverse coordinate, and that allows us to rewrite the system as ordinary differential equations in $\tilde{Y}$ alone. We write M and N as products of functions of T and $\tilde{Y}$. Substituting these products and Eq. (37) into Eqs (13) and (14), and requiring consistency in Eqs (13), (14) and Eq. (38), we find

$$M(Y,T) = \phi(T)^{1/2}\tilde{M}(\tilde{Y}), \tag{40}$$

$$N(Y,T) = \phi(T)^2\tilde{N}(\tilde{Y}), \tag{41}$$

$$\beta(T) = \phi(T)^2, \tag{42}$$

where the scaling $\phi(T)$ is given by

$$\phi'(T) = \left(\frac{\mathcal{P}}{\tilde{\mathcal{P}}}\right)^p \phi(T)^{p-1}, \tag{43}$$

and $\tilde{\mathcal{P}} = \int_{-\infty}^{\infty} \tilde{M}(\tilde{Y})^2 d\tilde{Y}$ is the input power in this reduced system. Here $\tilde{M}$ and $\tilde{N}$ are the shapes of the modal profile and the refractive index, which satisfy

$$\frac{1}{2}\tilde{M}''(\tilde{Y}) + (\tilde{N}(\tilde{Y}) - 1)\tilde{M}(\tilde{Y}) = 0, \tag{44}$$

$$2\tilde{N}(\tilde{Y}) + \tilde{Y}\tilde{N}'(\tilde{Y}) = \tilde{M}(\tilde{Y})^{2p}. \tag{45}$$

This reduced system can also be found by looking for scaling symmetries of Eqs (13) and (14) subject to Eq. (38) [37].

We have determined the shapes of the mode and refractive index by solving Eqs (44) and (45) numerically, results for which are shown in Fig. 12 for $p = 1$. For $p = 1$, we find $\tilde{\mathcal{P}} = 2.89$, and for $p = 2$, $\tilde{\mathcal{P}} = 2.94$. The solutions in Fig. 12 are the only single peaked solutions that decay as $\tilde{Y} \to \pm\infty$. For both $p = 1$ and $p = 2$, we find that the tails of the self-similar index profile decay as $\tilde{Y}^{-2}$ and that the tails of the mode decay exponentially. Combined with scalings (40)–(42) the solution in Fig. 12 is still the only known exact solution to the self-writing problem.

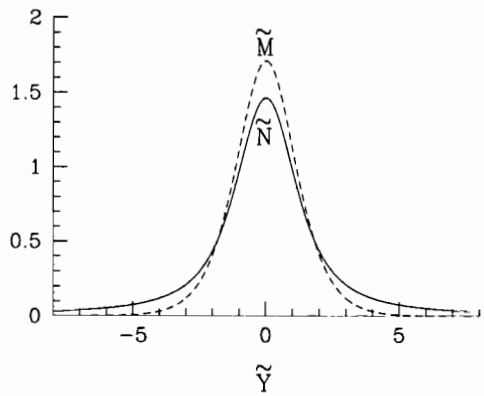

Figure 12: Similarity solutions of the self-writing problem ($p = 1$). $\tilde{M}$ Is the mode shape, $\tilde{N}$ the refractive index shape.

Recall that in deriving the solution in Fig. 12, the input beam is the mode of the evolving waveguide, and so it is time-varying. We now investigate whether the self-similar evolution can be related to the evolution of a waveguide produced by a time-independent input beam, which we take to be Gaussian [24]. Numerical simulations indicate that the shape of the index profile in the uniform waveguide region gives excellent agreement with Fig. 12. To test further the relationship between our solution and the simulations, we now investigate the scalings in Eqs (40)–(42).

For $p = 1$, Eq. (43) gives $\tilde{Y} \propto YT$, and so Eq. (41) predicts that the channel width w scales as T^{-1}. The numerical results shown in Fig. 13(a) confirm that $w^{-1} \propto T$ at different positions Z. The superior linearity at large Z is expected, since simulations [24] indicate that the waveguide is more uniform at larger Z.

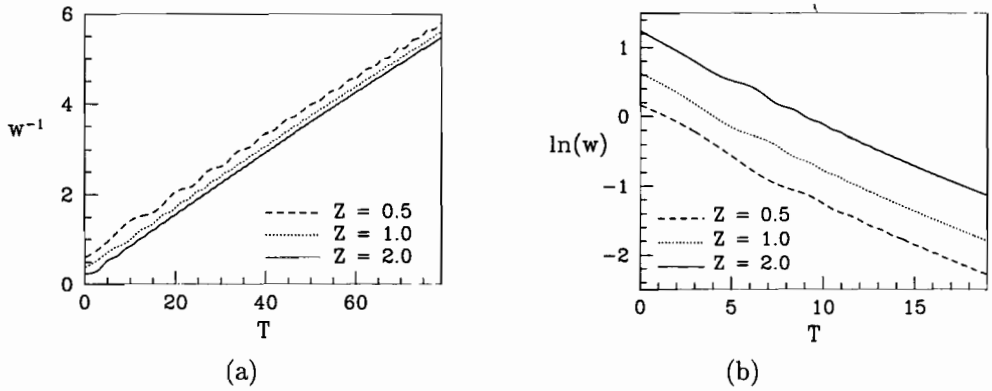

Figure 13: (a) Inverse width of the index versus T at different Z ($p = 1$). (b) Width of the index versus T on a log-linear plot at different Z ($p = 2$).

For $p = 2$, Eq. (41) predicts that $\ln w \propto T$. This is confirmed in Fig. 13(b), which shows $\ln w$ versus T at different Z positions. Numerical results for the peak refractive index also confirm scalings (41). Indeed, our numerical simulations indicate that the self-writing of a waveguide according to (13) and (14) appears to be very well described by the self-similar solutions. For brevity, the remainder of the results presented here are for $p = 1$.

For both $p = 1$ and $p = 2$, the agreement between predictions and simulations is similarly good for the depth of the channel as it is for the width. We now investigate the scaling prediction (42) for the propagation constant. Scalings (40)–(42) remain approximately valid when more than one mode is present, and are the same for each mode. Hence, the beat length Z_B scales as T^{-2} for $p = 1$. Fig. 14 shows $Z_B^{-1/2}$ versus T as given by the numerical simulation. This gives an approximately straight line, as predicted. No data is shown for $T \lesssim 15$ because the waveguide then does not support more than one symmetric mode.

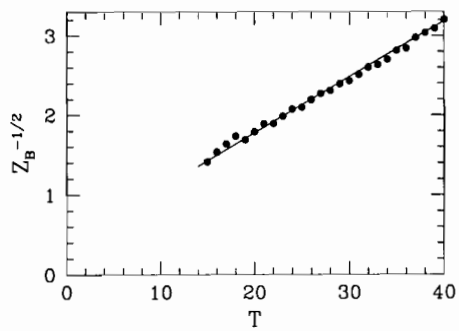

Figure 14: $Z_B^{-1/2}$ versus T ($p = 1$ simulation results), which gives a straight line, in agreement with the similarity prediction. The solid line is a straight line fit.

Hence not only does a self-similar solution exist; but it also describes simula-

tions of the full self-writing process well. This is remarkable: the input beam for the numerical simulation is a time-independent Gaussian, while the self-similar solution has a time-varying input. Note that the $\tilde{Y}^{-2}$ decay of the index profile implies that this system differs qualitatively from the seemingly related problem of spatial solitons [41].

The index profile is initially Gaussian, and its evolution into the predicted shape suggests that the self-similar solution is stable. We also investigated a triangularly shaped input intensity, and we again find that it evolves into the self-similar solution at larger Z. This further confirms the stability of the self-similar solution, and its relevance to a wide variety of self-writing processes.

4.3 Modal decomposition approach

Although the simulation in Section 3.1 is an important benchmark, it demands significant computational resources. Here an alternative technique is described in which the electric field and refractive index distributions are decomposed into modes. This technique is an efficient alternative to the full numerical simulation (see Ref. [25] for a fuller description). The use of modal decompositions to describe the propagation of light in waveguides is well established [42, 43, 17]. Decomposing the electric field into modes reduces the complexity of the problem, since the transverse dependence of the fields is described by the modes.

We make the following modal series expansions:

$$E(Y,Z,T) = \sum_{j=0}^{M-1} a_j(Z,T)F_j^{\beta}(Y), \qquad N(Y,Z,T) = \sum_{j=0}^{N-1} c_j(Z,T)F_j^{\beta}(Y) \quad (46)$$

where the a_j are complex functions and the c_j are real functions. The F_j^{β} are elements of a complete, orthonormal set of real basis functions, characterized by a free parameter β. In order for this technique to be numerically efficient, E and N need to be represented well using only a small number of basis elements.

Using the expansions in (46) in the photosensitivity equation and the paraxial wave equation, evolution equations for the modal coefficients a_j and c_j can be derived (see Ref.[25]). We choose the basis set to be even Hermite-Gaussian functions with a characteristic width β. These functions form a complete orthonormal basis set for even functions. The simulations in Section 3.1 clearly show that the width of a self-written waveguide is a strong function of time and position. Hence we adapt β to suit the evolving waveguide properties.

This method gives speed increases of two orders of magnitude for $p = 1$ and one order of magnitude for $p = 2$ when compared with the full numerical simulation. It typically also uses approximately one order of magnitude less computer memory. This significant speed increase makes it possible to investigate the waveguide formation process for a range of different initial conditions; this would not be feasible using the computationally slow full simulation. To demonstrate the power of this approach, we investigate Gaussian writing beams with a range of phase-front curvatures for $p = 1$. Fig. 15(a) shows the position

of the intensity primary eye as a function of the incident beam phase front curvature (d/z_R - see Ref. [25] for definition). The curves are the adaptive modal method predictions at different times, the dots are the corresponding simulation results. Excellent agreement is obtained over a wide range of curvatures; the modal method accurately predicts the eye position. It takes approximately three times longer to calculate the dots than it takes to calculate all the curves.

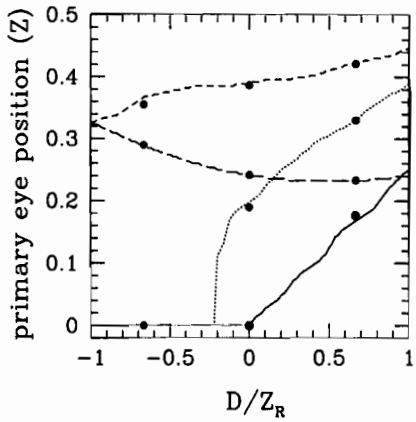

Figure 15: Position of the intensity primary eye as predicted by the modal method as a function of the incident beam curvature. Solid, dotted, small dashed and long dashed curves correspond to $T = 0, 0.01, 0.02, 0.1$. Large dots are simulation results.

The results presented here are for a planar geometry. As the increased efficiency of this modal approach arises from the simplification in the transverse dimension introduced by the modal functions, its efficiency relative to the full numerical simulation should be even more striking for the bulk case.

5 Self-written channels in glass

5.1 Key results

Here we describe the results of our self-writing experiment in planar germanosilicate glass (see Ref. [44]). We used an 11 mm long silica planar trilayer on a silicon substrate with a 3 μm thick photosensitive core layer containing 8% germanium. This layer was sandwiched between two undoped silica layers with a refractive index 0.022 lower than the core. This structure was grown using a HCPECVD process (see Section 1.2). The advantage of HCPECVD over conventional PECVD is its capability to produce low loss, non-porous germanosilica with high intrinsic photosensitivity [45].

We used a 0.5 W writing beam from a Argon-ion laser, emitting at a wavelength $\lambda = 488$ nm. The formation of a self-written channel relies on low-loss propagation of light through the material. The reason for using 488 nm light is

that losses are lower in the visible than in the near-UV, and are about 0.5 dB/cm in our sample. Using a microscope objective, the Gaussian beam is focussed to a spot size of 8 μm on the Ge-doped layer at the input edge of the sample. Another microscope objective images the beam from the sample's output edge onto a beam profiler. This setup is sketched in Fig. 16. We infer the refractive index evolution by monitoring the beam properties at the output edge.

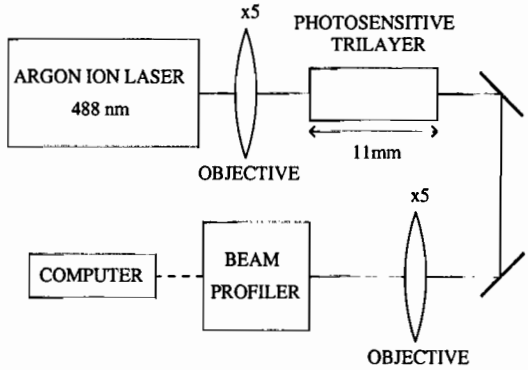

Figure 16: Setup used to self-writing of a channel in photosensitive glass.

As self-writing proceeds and a channel forms, the evolving index change counteracts the writing beam's diffraction. Hence the beam width at the output edge of the sample should decrease over time, and the peak intensity should increase. As Fig. 17 shows, we do observe this behavior; the beam becomes dramatically narrower and more intense during the exposure. This is the key indication that a channel forms in the originally uniform slab waveguide. Note that the beam sits on an unchanging pedestal, which we believe corresponds to light guided by the superstructure formed by the cladding, core and substrate. We found that the pedestal evident in Fig. 17 could be eliminated after the exposure by optimization of the coupling into the waveguide. This further supports the hypothesis that the pedestal is caused by light in a mode of the superstructure.

5.2 Beam evolution

Here the evolution of the beam at the output edge during the self-writing is presented in more detail. The solid line in Fig. 18 shows the full width at half maximum (FWHM) of the intensity profile at the output edge of the trilayer as a function of time. The beam narrows by a factor of 14 in 8 hours, reducing in width from 210 μm to 15 μm. By comparison with our simulations, we infer that this beam width corresponds to a channel waveguide with a FWHM of approximately 23 μm.

The peak intensity of the beam as a function of time (relative to the initial peak intensity) is given in Fig. 19. For the first four hours, the peak intensity

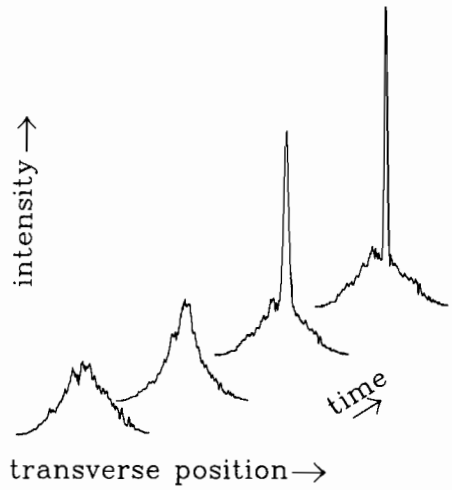

Figure 17: Beam intensity profiles at the output edge at 0, 0.5, 3 and 8 hrs respectively from the start of the exposure.

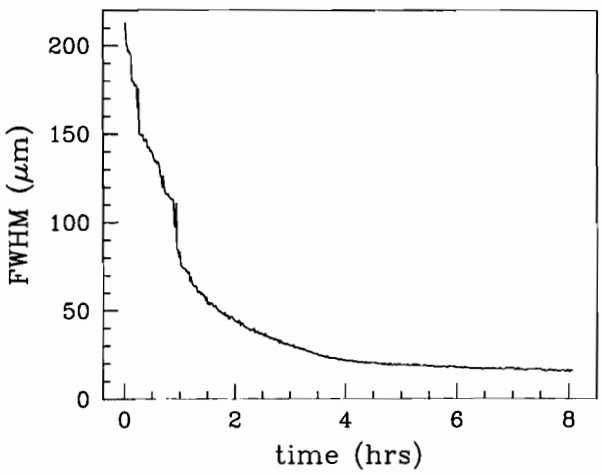

Figure 18: FWHM at the output edge versus time. The beam narrows, indicating that a channel is forming in the material.

increases, as predicted. When a factor of roughly 10 width decrease has occurred, the peak intensity flattens out, and remains approximately constant for the remainder of the experiment. It is interesting to note that the beam width continues to narrow somewhat after the intensity has saturated.

As noted above, although the width decreases by a factor of 14, the peak intensity only increases by a factor of 4. Using numerical simulations, we infer that this is caused by increased attenuation in the material during exposure

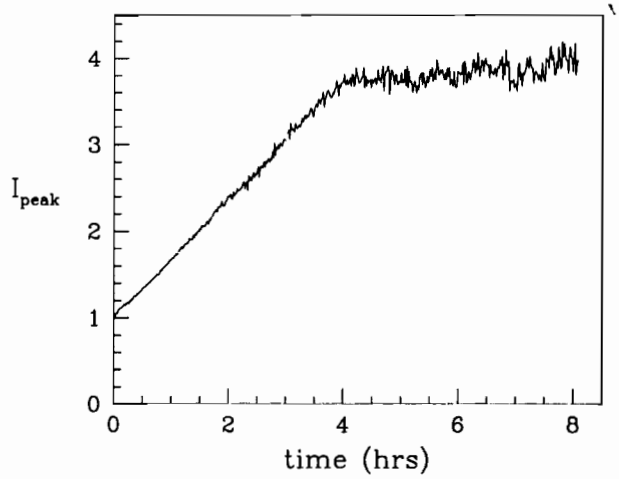

Figure 19: Peak intensity at the output edge versus time.

(see Section 5.3). Other properties of the self-written channel are explored using luminescence in Section 5.4.

5.3 Comparison with simulations

This section compares the experimental results presented in Section 5.2 with the theoretical predictions. For the numerical simulations to make accurate quantitative predictions for the self-written evolution, it is necessary to include the effects of saturation of the refractive index change (Δn_s). If saturation is ignored, the model predicts that the peak intensity increases without bound, which is clearly unphysical. We have used the value $\Delta n_s = 0.001$, which is a typical value for this material [45]. The dotted line in Fig. 20 shows the predicted beam width at the output edge as calculated using the simulation with this saturation index value (the solid line is the experimental result from Fig. 18). The numerical result allows for a single adjustable parameter, corresponding to a linear scaling of time. This scaling was chosen to give the best visual agreement with experiment. Clearly, the qualitative agreement with the experimental results (solid line) in Fig. 18 is good.

As described in Section 3.2.2, shortly after the primary eye forms, the self-written waveguide supports two even modes which beat, resulting in intensity maxima which move along the propagation axis over time (the secondary eyes). The plateau-like features in the dotted curve in Fig. 20 are caused by secondary eyes moving past the measurement position. The experimental results (solid line) also exhibit a number of such features, which are likely to be caused by the movement of these secondary eyes.

The dotted line in the inset in Fig. 21 shows the simulation prediction for the peak intensity which corresponds to the width prediction shown in Fig. 20. Although the simulation gives roughly the right qualitative behaviour for the

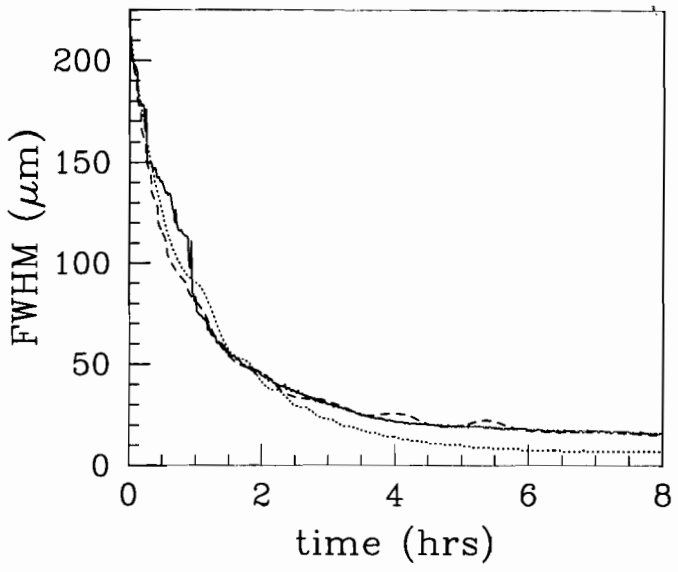

Figure 20: FWHM of the beam at the output edge. The solid line is the experimental result from Fig. 18, dashed and dotted lines show theoretical predictions.

evolution of the peak intensity, the predicted increase in the intensity is a factor of ten larger than observed, and the qualitative agreement between dotted and solid lines in Fig. 20 is correspondingly poor.

In the simulation predictions shown using dotted lines in Figs. 20 and 21, the material attenuation was ignored. However, if material losses are taken to increase with exposure as in Eq. (10), the discrepancies between the predictions and the experimental results can be significantly reduced.

The dashed lines in Figs 20 and 21 are numerical simulation results which include the effect of exposure-dependent losses. The same saturation value as above was used, and $\gamma = 0.05$ [see Eq. (10)]. This value of γ was chosen to optimize the agreement with experiment; note that the dashed and solid lines are almost indistinguishable in Fig. 20. It also leads to good quantitative agreement for the peak intensity, as Fig. 21 shows a much improved prediction for the magnitude of the intensity change during exposure. This choice of γ also improves the prediction for the time at which the intensity flattens out. From these results we are confident that significant changes in attenuation occur during the exposure, and that they are the reason why the peak intensity only increases by a factor of 4 whilst the width decreases by a factor of 14.

The simulation has oscillations in the peak intensity that are not experimentally observed. It is probable that these can be explained by adding more effects to our model. Such extra refinements are not pursued here.

Hence by including the effects of saturation and an exposure-dependent attenuation in our model, we obtain quantitative agreement with observations for

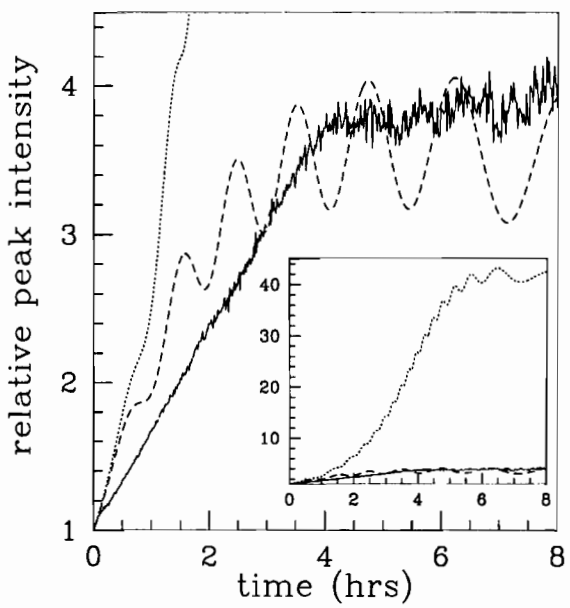

Figure 21: Evolution of the peak intensity at the output edge. The solid line is the experimental result from Fig. 19, dashed and dotted lines show theoretical predictions.

self-writing. The value of Δn_s can only be altered to within a few percent if this level of quantitative agreement is to be maintained. However, the value of γ is less tightly constrained.

The value $\Delta n_s = 0.001$, the maximum possible index change in our model [see Eq. (14)], was chosen because it is a typical value for the saturation index in this material. As we assume here that the loss increases in proportion to the local index change, this imposes a saturation value on the attenuation coefficient also. Using Eq. 10, the saturation value of the loss is $\alpha_s = \gamma k_0 \Delta n_s$, which for the values here is equivalent to roughly $3\,\mathrm{dB\,mm^{-1}}$. The loss only reaches this level in regions where the refractive index change approaches saturation. The average or effective loss and the local loss further along the channel are substantially less than this maximum value.

5.4 Channel properties

As shown in Section 5.3, when the effect of exposure-dependent attenuation is included, the numerical simulations make excellent predictions for the evolution of the beam at the output edge. Although numerical predictions can be made for the intensity everywhere in the material, it is somewhat more difficult to extract this information during the experiment. However we observed that when the material is illuminated with 488 nm light, it exhibits strong red luminescence [44], similar to that previously observed in germanosilicate preforms and fibers

[46]. This luminescence gives an indirect indication of the light intensity within the material. If the channel is exposed using low intensity levels, then it does not evolve further. The luminescence distribution contains detailed information about the intensity within the material. We show here that the luminescence distribution in the material can be used to confirm some of the more subtle features are also predicted by the theory.

Fig. 22 shows a photograph of the luminescence distribution at an unexposed position on the trilayer, taken from above. The sample is illuminated by a low-intensity beam at 488 nm which is focused onto the sample edge. Light is incident from the left of the photograph, and a filter was used to block out the writing wavelength.

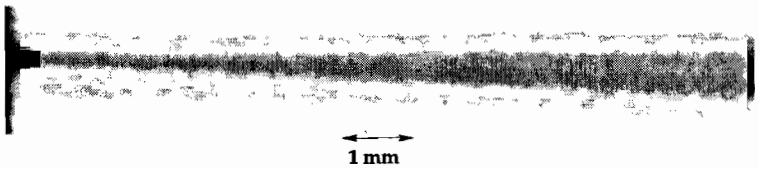

Figure 22: Photograph of the luminescence taken from above. Light is incident from the left. There is no channel waveguide at this position, and the beam simply diffracts.

Fig. 23 shows the luminescence at the position where the original exposure occurred. The beam width at the right edge is clearly smaller than in Fig. 22. Note that Fig. 23 displays a waist region approximately 0.45 mm from the input face. In the dimensionless coordinates, this corresponds to a distance $Z \approx 0.5$ [see Eq. (12a)]. This distance is consistent with the typical distance between the primary eye and the input face (see Fig. 5). Hence we infer that the waist is the intensity primary eye.

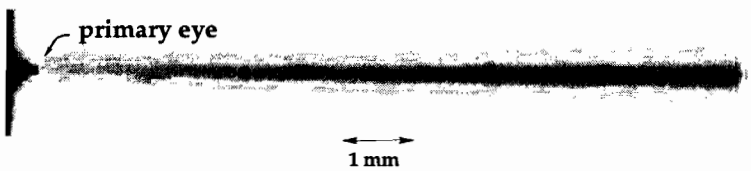

Figure 23: As for Fig. 22 except that this photograph is at the self-written channel position, where the beam confinement is much improved.

Fig. 24 shows the same data as Fig. 23, except that the contrast has been adjusted and the vertical axis has been expanded by a factor of three for clarity. Fig. 24 displays five regions of high intensity, and we identify these to be the secondary eyes predicted by the theory. The maxima become more widely spaced further from the input face. This is also consistent with the theoretical predictions for this two-photon process (see Section 3.2.2). Hence the luminescence distribution reveals the spatial features predicted by the theory.

Some aspects of the luminescence appear to be inconsistent with the ex-

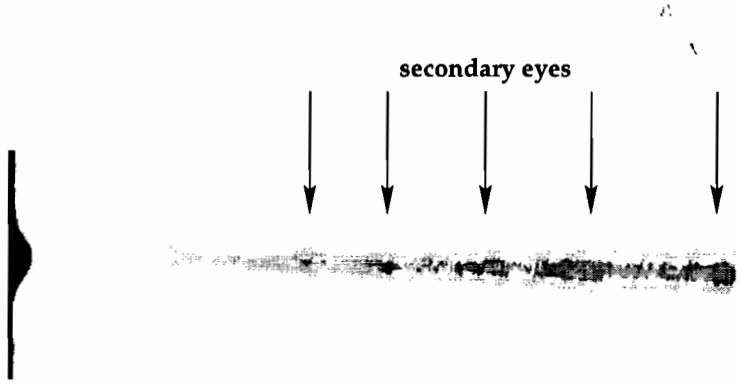

Figure 24: The data from Fig. 23 expanded by a factor of three vertically. The arrows indicate regions of high intensity, and the contrast has been increased.

pected intensity distribution. For example, contrary to expectation, the primary eye appears as a region of low luminescence, even though it is the point of highest light intensity. Previous work has shown that the luminescence of germanosilicate glass can decrease with cumulative exposure [47], which probably explains why the brightness of the luminescence is low around the primary eye. However, unlike the primary eye, the secondary eyes do appear as regions of high luminescence. This is because the photosensitive-induced changes to the luminescence caused by the secondary eyes are not localised at their maxima. Instead, because the secondary eyes move relatively rapidly along the axis, they decrease luminescence on the axis in a uniform manner. Thus the brightness of the luminescence remains proportional to the intensity distribution.

In future experiments, more rigorous tests of the theoretical predictions could be made by monitoring the luminescence *in situ*. In particular, by observing the way in which the secondary eyes move during the exposure, the details of the model could be fine-tuned.

5.5 Modal properties

As described in Section 5.4, secondary eyes are observed when the channel is illuminated with 488 nm light. Since secondary eyes are caused by mode beating, this implies that the waveguide is multimoded at this wavelength. Furthermore, as the channel is effectively permanent, it can be used to guide light at other wavelengths; the channel should be single-moded at 1550 nm [24], and, for example, multi-moded at the shorter wavelength of 633 nm. We have confirmed that the channel is single-moded at 1550 nm by coupling light from a diode laser into the channel and recording the far-field intensity pattern, which is shown in Fig. 25(a). As expected, the distribution is single-peaked, and was found to be insensitive to the launch conditions, which together imply that the channel is single-moded. We also confirmed that the channel is multimoded at 633 nm using light from a He-Ne laser. In this case, the far-field distribution is multiply-peaked as shown in Fig. 25(b). In addition, this distribution exhibits

the expected large sensitivity to the launch conditions at this wavelength.

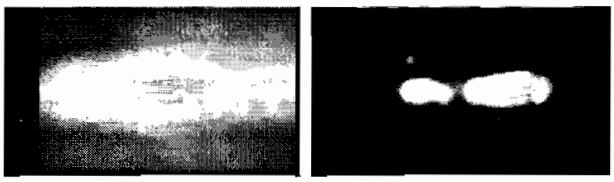

(a) (b)

Figure 25: The far-field intensity pattern when the self-written channel is used to guide (a) 1550 nm light (b) 633 nm light.

Note that the photographs from the previous section were taken two weeks after the original 8 hour exposure. In addition, the far-field patterns in Fig. 25 were recorded six months after the original exposure, further evidence for the effectively permanent nature of the self-written channel.

6 Related work

Self-writing processes can occur in a range of materials and geometries. To date, the process which has been studied in greatest detail (both experimentally and theoretically) makes use of germanium-silicate planar waveguides, and these results were discussed in detail in Sections 2 - 5. In this section, we review other self-writing experiments which have been done to date.

6.1 Uptapers in UV-cured epoxy

In 1993 Frisken [1] showed that permanent waveguide uptapers can be formed in UV-cured epoxy using 532 nm light. A sketch of this process is shown in Fig. 26. Frisken used a commercially available epoxy (containing acrylic acid and hydroxypropyl methacrylate) which exhibits permanent refractive index changes in response to light at 532 nm. Initially the material has a uniform refractive index and the experiment the light is confined in two dimensions.

Frisken observed that the far-field spot size of the beam reduced by a factor of ten during the exposure. This indicates that a waveguide uptaper forms in the following way: initially, light in the fundamental mode of the fibre diffracts into the epoxy. As the spot size at the beam waist is small, the beam diffracts rapidly, and the far-field spot size is large [Fig. 26(a)]. The refractive index changes most in the beam waist region, where the intensity is highest, and an adiabatically tapered index distribution is created by the diffracting beam. This tapered index distribution guides the light further into the material, gradually increasing the size of the beam waist with distance from the fibre edge. Hence the beam emerging from the tapered region diffracts less rapidly, and so the far-field spot size should decrease. Over time this process continues and a waveguide uptaper forms [Fig. 26(b)].

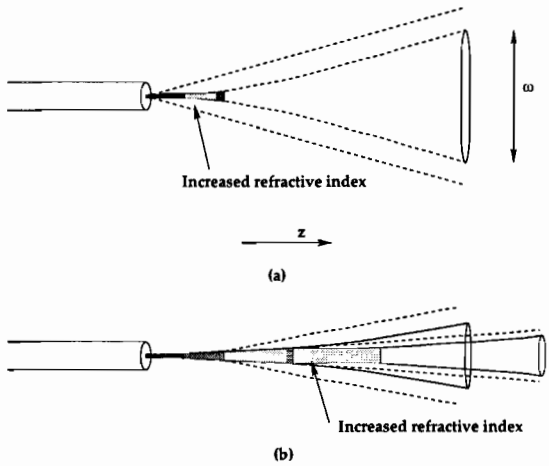

Figure 26: (a) Light diffracts from a fibre into the epoxy; the refractive index changes most rapidly in the beam waist. (b) A waveguide uptaper forms in the epoxy [1].

In this experiment the beam of light *self-writes* the uptaper which guides it through the epoxy, and as the index changes are long-lasting, uptapers written in this way can subsequently be used at other wavelengths. Indeed this process is closely related to the early evolution of a self-written waveguide in photosensitive glass (see Section 3 for a detailed exposition of the waveguide evolution). If the experiment conducted by Frisken was allowed to continue for longer times, we expect that the dynamics of the process would resemble the self-writing process described in Section 1.1 more closely.

Uptapers can be used to reduce insertion losses when bulk devices are integrated with fibre devices. They do this by adiabatically changing the size of the mode from a fibre so that coupling to a bulk device or a fibre with a different mode diameter is optimized.

6.2 Self-trapping and self-focusing in photopolymers

Some liquid polymers, referred to as *photopolymers*, also exhibit permanent refractive index changes in response to light. Refractive index changes as large as $\Delta n_s = 0.15$ have been observed [48], significantly larger than the changes achieved to date in photosensitive glasses. Kewitsch *et al.* [32, 29] showed that using *photopolymerization*, self-trapping and self-focusing can be demonstrated in a liquid diacrylate polymer. Refractive index changes caused by photopolymerization are better understood than glass photosensitivity, and the mechanism behind photopolymerization is outlined briefly here [32].

When a photopolymer is illuminated with light of appropriate wavelength (*i.e.* 325 nm in a diacrylate polymer), the polymer chains begin to join. The polymer density is closely related to the lengths of these chains. The density increases with increasing chain length, as the polymer becomes more tightly

packed. Initially the polymer chains are short, and so illumination produces only a small change in density, and hence effectively no change in the refractive index. In the next stage of photopolymerization, much larger chains form, and so illumination produces large refractive index changes as entire polymer backbones join. Hence it takes time for the polymer chains to grow large enough to change the refractive index, which causes the index changes to be delayed by a diffusion time $\tau = 0.01$ to 1 s relative to the illumination. Kewitsch et al. used a diacrylate polymer in which $\tau = 0.1$ s. In the final stage, few polymer chains remain free to join, and the polymer has solidified in the exposed regions.

The model for the index change in a photopolymer given in Ref [32] can be written in the same form as Eq. (9), and this model agrees well with observations from Ref [32]. Hence although photopolymerization is clearly different from glass photosensitivity on a microscopic scale, phenomenologically it can be modelled in the same way as one-photon glass photosensitivity.

Using numerical simulations of the kind described in Section 3.1, Kewitsch *et al.* showed that *self-focusing* occurs in a planar polymer structure. In these simulations [32], a Gaussian beam was focused to a waist inside the planar layer. When the material is illuminated continuously for 30 s the waist moves towards the input face, which was considered to be a manifestation of self-focusing.

In the experiment by Kewitsch *et al.* [32, 29], light at 325 nm was incident on a liquid diacrylate polymer. At the input face, the diameter of the beam was 100 μm. The polymer was given a series of short exposures, each separated by a time larger than the diffusion time, τ. This was done to ensure that the polymer did not completely cure in the exposed region before the writing beam experiences the index change. These exposures cause a fibre-like structure to form inside the liquid polymer. Kewitsch *et al.* moved the writing beam to form a grid of these fibres in the polymer. Each fibre was roughly 1 cm long, and was observed to guide the writing beam over this distance.

The self-focusing and self-trapping described above are both closely related to the self-writing process described in Section 1.1. The movement of the beam waist observed in the self-trapping simulations is analogous to the *primary eye* discussed in Section 3. In the self-focusing simulation in Ref. [32], τ is negligible compared with the exposure time. In this limit, the model used for photopolymerization reduces to the simple one-photon model for photosensitivity used in Section 2. So even though the microscopic details of these processes are completely unrelated, on a phenomenological level they are equivalent. Hence the theoretical analysis of self-writing in a planar photosensitive material described in Section 4 can also be applied to self-focusing in a diacrylate polymer. The self-trapping process described by Kewitsch *et al.* is analogous to self-writing in bulk photosensitive glasses.

When τ becomes significant when compared with the time-scale for the waveguide evolution, the close analogy between self-focusing, self-trapping and self-writing in photosensitive glasses breaks down. However, many of the techniques developed to study self-writing in photosensitive glass can still be applied. For example, the series expansion technique described in Section 4.1 has been used to explore the effect the delay in the material response has on the primary eye

dynamics (see Ref. [27]).

6.3 Self-writing in planar chalcogenide glass

The experiments described in Sections 6.1 and 6.2 both occur in bulk materials. The experiment presented in Section 5 was the first self-writing experiment in a planar geometry, and was also the first observation of self-writing in glass. More recently, Meneghini *et al.* observed self-writing in As_2S_3 thin films [49, 50]. This process resembles the process in Section 5 very closely, because it also makes use of a planar writing geometry. Chalcogenide glasses such as As_2S_3 can experience very large photosensitive refractive index changes [51].

In this recent experiment, a mode locked Ti:sapphire laser operating near 800 nm was used to end-fire ~100 fs pulses into a planar waveguide using a cylindrical telescope with an 8:1 aspect ratio and a 10× microscope objective. At this wavelength chalcogenide glass experiences a photosensitive response which can be modelled well as a two-photon process [49]. The propagation distance was 4 mm and the beam width at the edge of the sample was 13 μm. After roughly 10 minutes exposure, Meneghini *et al.* observed that the width at the output edge of the sample had contracted noticeably, and the peak intensity had increased by a factor of two. The growth curves for the intensity also display the same type of oscillations as in Section 5.3, Fig. 21, indicating the presence of loss. This is a clear indication that the writing beam forms a self-written channel in this material.

As the refractive index change in this chalcogenide glass is a two-photon process in a planar material, all the theoretical techniques presented in Sections 3.1 - 4.2 can be applied directly to this self-writing process.

6.4 Growing fibres in photopolymerizable resins

Shoji and Kawata [52] have self-written fibres in a phtopolymerizable resin consisting of urethane acrylate monomers and oligomers accompanied by photoinitiators using 441.6 nm light from a He-Cd laser. In addition, to single fibres which grow in a way similar to that seen by Kewitsch and Yariv [32, 29], they have also investigated the dynamic evolution of multiple self written fibres. They observed that depending on the angle of intersection, two self-written fibres might either merge into a single fibre or cross without merging. For example, in their experiments the self-written fibres merged only when the angle of intersection was less than 9°. The coherence relationship between the two incident beams does not effect the merging phenomenon.

6.5 Self-writing in undoped glass

Recently, Homoelle *et al.* [53] induced refractive index changes in both pure and boron-doped fused silica by exposure to femtosecond infrared laser pulses. They have achieved index changes as a large as 5×10^{-3} using a multipass Ti:Sapphire

amplifier emitting at 820 nm. Although the physical mechanism is not understood, it is apparently a high order multiphoton absorption process and exhibits a highly nonlinear dependence on the intensity. The observation that final saturation levels are comparable to those obtained with UV photosensitivity and that the annealing properties are also similar suggests that the infrared absorption may be initiating the same final microscopic changes as the UV but via a different initial pathway. It may be possible to analyze self-writing with this process using the phenomenological model in Section 2.3, but with $p = 5$ or 6. The differences observed between the one- and two-photon models would be expected to be greatly amplified in the multiphon case. The high nonlinearity allows for the fabrication of highly localised detailed structures by, for example, translation of the sample with respect to the focal point. Three dimensional photonic circuits can also be fabricated by this means.

6.6 Other self-action effects

As self-writing proceeds, the initial diffraction of the beam is overcome by the refractive index change it induces. Spatial solitons and photorefractive solitons are also formed by *self-action* effects, where diffraction is balanced by light-induced index changes. Although self-writing is closely connected with these self-action effects, there are a number of quite fundamental differences which distinguish them, as highlighted in Sections 6.6.1 and 6.6.2.

6.6.1 Spatial solitons

An intense optical beam causes the refractive index of silica glass to alter locally in an instantaneous, non-cumulative way according to the optical Kerr effect

$$n(t) = n_0 + n_2 |E(t)|^2, \tag{47}$$

where n_0 is the low-intensity refractive index of the material, n_2 is a constant which characterises the strength of the nonlinearity [54] and E is the electric field. In silica this is an intrinsic property of the material that does not depend on the presence of doping. A low intensity beam incident on a planar material diffracts. A high intensity input beam causes the refractive index to increase via the optical Kerr effect if $n_2 > 0$ [see Eq. (47)]. This process is described by the nonlinear Schrödinger equation. The soliton solutions to this equation, corresponds to *spatial solitons*, which do not change shape upon propagation, by balancing the Kerr effect and diffraction.

Spatial solitons were first observed in CS_2 liquid by Barthelemy *et al.* in 1985 [55]. The first observation of spatial solitons in glass waveguides was made by Aitchison *et al.* [33] in 1990. Glass has a low value of n_2, and so high intensities ($\approx 1\,\mathrm{MW\,cm^{-2}}$) are required. More recently, it has been shown that spatial solitons can also exist in materials with a quadratic nonlinearity, *i.e.* where the nonlinear polarization depends quadratically on the applied field [56].

Superficially, the formation of spatial solitons seems to be similar to the self-writing process presented in Section 1.1. In each case, the diffraction of the input

beam is overcome by a region of increased refractive index, or, more generally, a region with a positive nonlinear contribution to the phase, induced by this beam. However, here the similarity ends. The effects induced by the quadratic and Kerr nonlinearities are instantaneous and non-cumulative. When the light is removed, the effects disappear, and so the material is unchanged after the passage of an intense beam of light. This differs fundamentally from photosensitivity, where the refractive index changes are permanent, and hence cumulative. The beam is not instantaneously guided by a self-written waveguide; it takes time for the waveguide to evolve.

6.6.2 Photorefractive solitons

In photorefractive (PR) materials, such as lithium niobate ($LiNbO_3$) or strontium barium niobate (SBN), light can be used to pattern long-lasting refractive index structures. When a PR crystal is exposed to light, free charge carriers are excited, which are then free to diffuse, leaving behind fixed charges of the opposite sign. Ionised impurities at other locations can then trap the carriers. Thus an inhomogeneous space-charge distribution forms in the crystal which mirrors the intensity distribution, and this remains after the light is switched off [16]. This space-charge distribution creates an electric field which modulates the local refractive index via the electro-optic effect. The material can be restored to its original state by uniform illumination at the writing wavelength or by heating. This effect is by nature non-local, because before the carriers are trapped, they are free diffuse within the material. This contrasts the photosensitivity effect, for which local models are adequate, and this leads to fundamental differences between these processes.

In 1992, Segev *et al.* [57] proposed a new type of photorefractive spatial soliton which can form when an external electric field is applied to the crystal. This effect is independent of the absolute light intensity, and so photorefractive solitons can be generated at low intensities ($< 0.2\,\mathrm{W\,cm^{-2}}$), unlike spatial solitons, for which intensity of $1\,\mathrm{MW\,cm^{-2}}$ are required [58]. Also, unlike spatial solitons, photorefractive solitons do not appear instantaneously, and take time to evolve. Experiments by Duree *et al.* [58, 59] confirmed the predictions of Segev *et al.*, showing that solitons can be formed using the PR effect. These solitons are quasisteady and exist only for a finite time (up to 10 s) before the electric field begins to be screened by the electric field in the material [59]. These solitons can act as waveguides; for example Morin *et al.* [60] showed that a weak PR soliton can guide an intense beam at a longer wavelength at which the material is not photorefractive.

The PR solitons described thus far resemble self-written waveguides in the sense that the light-induced index changes counteract the usual diffraction of the beam. However, as described above, these solitons are by nature transient; as soon as the external electric field begins to be screened out these solitons are destroyed. In contrast, the waveguides produced using self-writing in a photosensitive material last many years.

More recently, Christodoulides *et al.* [61] discovered a new class of non-

diffracting beams in unbiased planar PR materials. The solutions have the form of an exponentially decaying Airy function. However, to observe this non-diffracting behaviour, the input beam must match this form extremely closely. Contrastingly, any single-peaked input beam can be used to self-write a channel in a photosensitive material.

Segev *et al.* predicted the existence of *screening solitons* in PR materials [62], and they were observed in bulk SBN by Shih *et al.* [63]. When an external electric field is applied, non-uniform screening effects cause the field magnitude to decrease in regions of high intensity. Again, the index is modified via the electro-optic effect, and traps the beam [62]. Solitons formed in this way differ from those discussed above; in particular although the PR effect is non-local, the non-uniform screening effect is itself local. Also, screening solitons are steady state solitons, whereas the solitons described above are transient. Screening solitons are thus the PR solitons which bear the closest resemblance to self-written waveguides both because they are the result of a local effect, and because they are long lasting. However, if the external field is switched off, the index distribution in the material disappears on the time-scale of the dielectric relaxation time (typically about 1 s) [64].

7 Discussion and conclusions

This review makes it clear that self-writing is a generic phenomenon that can be observed in a range of materials. Many of the features observed in photosensitive glass can be understood quantitatively using the phenomenological model (11) discussed here, provided that it is augmented by the dose-dependent loss term (10). It is clear that in this way the detailed properties of self-written waveguides can give information about the material's response to light. This procedure was already used to ascertain the validity of the local model two-photon (8) from self-written grating experiments, at least for small refractive index changes [21, 22]. Similarly, in the future a comparison of the far-field intensity distribution in a self-written channel with the self-similarity predictions from Section 4.2 should provide further information about the material's response to illumination.

While the experiments discussed here in some detail led to the formation of single channels in a planar structure, the work by Shoji and Kawata [52] shows that more complex structures, such as X- and Y-junctions, can be written. Though in their work the number of channels that evolves cannot always be predicted, our results imply that by careful experimental procedure, complex, self-written structures can be designed. For such structures, the advantages of self-writing over more conventional techniques may be greater than for single channels, since once the input beam is identified, the dynamics of the self-writing take control of the refractive index evolution. Another extension of our work will be the generalization to bulk glass, following earlier work in bulk polymers by Frisken [1] and Kewitsch and Yariv [32, 29]. Regardless of these details, the model that we have established gives a good description of the self-writing

process, and we are confident that it will be a good predictor in this future work.

One of the key problems with our experimental work is that the experiments take about 8 hours, as shown in Figs 18 and 19. There are a number of obvious ways in which this can be improved. First, since we are using a local two photon model for photosensitivity we expect the rate at which the writing occurs to be proportional to the square of the intensity. Thus, the writing process can be shortened by increasing the incident beam power, or preferably, by optimizing the coupling into the waveguide using an elliptically shaped incident beam as done by Meneghini *et al.* [49, 50]. Their work shows another way to achieve short writing times, using very photosensitive chalcogenide glasses, in combination with the use of a high peak-power, short-pulse laser (Sect. 6.3).

The two main theoretical techniques used, that based on a Taylor series (Section 4.1) and a similarity solution (Section 4.2) are complementary in that they give good description of the evolution in the near field and in the far field, respectively. While they have greatly enhanced understanding, neither of the two methods gives an adequate description of the primary eye in a mature waveguide. This is unfortunate, since the primary eye essentially marks the beginning of the waveguide channel and seems to determine, for example, how much light enters each of the modes of the channel, once it is multi-moded. It thus, indirectly, determines the strengths of the secondary eyes. More theoretical work is needed in this area. We believe the key to this is a suitable generalization of the Taylor series expansion, some of which were explored in Section 4.1.3.

In conclusion, the self-writing of permanent waveguides has been demonstrated using a number of different geometries and materials. While the theoretical understanding of the writing process is good, the present lack of understanding of the primary eye may affect progress. Though the structures that have been written thus far are fairly simple, there is no doubt that more complex, and potential useful and interesting structures and devices will be able to be fabricated in this way. The future for self-written waveguides is bright!

8 Acknowledgements

When this work was done, Tanya Monro was with the School of Physics, University of Sydney, and the Australian Photonics Cooperative Research Centre. Leon Poladian acknowledges the financial support of the Australian Research Council. The authors are grateful to Michael Bazylenko, Robert Charters and Jesper Arentoft for the provision of samples and also to David Moss and Peter Miller who collaborated on part of the project. We also thank Graham Atkins, John Canning, Steve Frisken, Peter Krug, Peter Hill, Simon Fleming and John Sipe for discussions.

References

[1] S. J. Frisken, 'Light-induced optical waveguide uptapers,' Opt. Lett. **18**, 1035 – 1037 (1993).

[2] A. Roberts, M. L. von Bibra and J. N. Walford, 'Fabrication of buried channel waveguides using focussed MeV proton irradiation,' in *Ion beam modification of materials* (Eds. J. S. Williams, R. G. Elliman and M. C. Ridgway) (Elsevier, 1996), Proceedings of the Ninth International Conference of Ion Beam Modification of Materials, 968 – 971.

[3] K. O. Hill, Y. Fujii, D. C. Johnson and B. S. Kawasaki, 'Photosensitivity in optical fiber waveguides: Applications to reflection filter fabrication,' Appl. Phys. Lett **32**, 647 – 649 (1978).

[4] D. K. W. Lam and B. K. Garside, 'Characterization of single-mode optical fiber filters,' Appl. Optics **20**, 440 – 445 (1981).

[5] G. Meltz, W. W. Morey and W. H. Glenn, 'Formation of Bragg gratings in optical fibres by a transverse holographic method,' Opt. Lett. **14**, 823 – 825 (1989).

[6] B. Malo, K. A. Vineberg, F. Bilodeau, J. Albert, D. C. Johnson and K. O. Hill, 'Ultraviolet light photosensitivity in Ge-doped silica fibers: wavelength dependence of the light-induced index change,' Opt. Lett. **15**, 953 – 955 (1990).

[7] M. Svalgaard, C. V. Poulsen, A. Bjarklev, and O. Poulsen, 'Direct UV writing of buried singlemode channel waveguides in Ge-doped silica films,' Elect. Lett. **30**, 1401 – 1403 (1994).

[8] C. V. Poulsen, J. Hubner, T. Rasmussen, L. Anderson and M. Kristensen, 'Characterisation of dispersion properties in planar waveguides using UV-induced Bragg gratings,' Elect. Lett. **31**, 1437 – 1438 (1995).

[9] D. J. Moss, J. Canning, M. Faith, S. Madden, P. Kemeny, L. Poladian, F. Ladouceur, J. D. Love, C. V. Poulsen and O. Leistiko, 'Ultra-strong UV written gratings in PECVD grown germanosilicate waveguides,' in *Photosensitive Optical Materials and Devices* (1997), vol. 2998, 142 – 145.

[10] K. Tanaka, N. Toyosawa and H. Hisakuni, 'Photoinduced Bragg gratings in As_2S_3 optical fibers,' Opt. Lett. **20**, 1976 – 1978 (1995).

[11] M. M. Broer, R. L. Cone and J. R. Simpson, 'Ultraviolet-induced distributed-feedback gratings in Ce^{3+}-doped silica optical fibers,' Opt. Lett. **16**, 1391 – 1393 (1991).

[12] K. O. Hill, B. Malo, F. Bilodeau, D. C. Johnson, T. F. Morse, A. Kilian, L. Reinhart and K. Oh, 'Photosensitivity in Eu^{2+}:Al_2O_3-doped-core fiber: Preliminary results and application to mode converters,' in *Optical Fibre Communications Conference, OFC'91, Technical Digest* (1991), 14 – 17.

[13] K. O. Hill, B. Malo, F. Bilodeau and D. C. Johnson, 'Photosensitivity in optical fibres,' Ann. Rev. Matter. Sci. **23**, 125 – 158 (1993).

[14] M. Douay, W. Xie, T. Taunay, P. Bernage, P. Niay, P. Cordier, B. Poumellec, L. Dong, J. F. Bayon, H. Poignant and E. Delevanque, 'Densification involved in the uv-based photosensitivity of silica glasses and optical fibers,' J. Lightw. Tech. **15**, 1329 – 1342 (1997).

[15] T. Erdogan, V. Mizrahi, P. J. Lemaire and D. Monroe, 'Decay of ultraviolet-induced fiber Bragg gratings,' J. Appl. Phys. **76**, 73 – 80 (1994).

[16] B. E. A. Saleh and M. C. Teich, *Fundamentals of Photonics* (Wiley, 1991).

[17] R. März, *Integrated Optics: Design and Modeling* (Artec House, 1995).

[18] C. M. de Sterke and J. E. Sipe, 'Ideal mode expansion for planar optical waveguides,' J. Opt. Soc. Am. A **7**, 636 – 645 (1990).

[19] A. E. Siegman, *Lasers* (University Science Books, 1986).

[20] D. P. Hand and P. S. Russell, 'Photoinduced refractive-index changes in germanosilicate fibers,' Opt. Lett. **15**, 102 – 104 (1990).

[21] V. Mizrahi, S. LaRochelle, G. I. Stegeman and J. E. Sipe, 'Physics of photosensitive-grating formation in optical fibers,' Phys. Rev. A **43**, 433 – 438 (1991).

[22] C. M. de Sterke, S. An and J. E. Sipe, 'Growth dynamics of phase gratings in optical fibres,' Opt. Comm. **83**, 315 – 321 (1991).

[23] P. A. Krug, R. Stolte and R. Ulrich, 'Measurement of index modulation along an optical fibre bragg grating,' Opt. Lett. **20**, 1767 – 1769 (1995).

[24] T. M. Monro, C. M. de Sterke and L. Poladian, 'Investigation of waveguide growth in photosensitive germano- silicate glass,' J. Opt. Soc. Am. B **13**, 2824 – 2832 (1996).

[25] T. M. Monro, C. M. de Sterke and L. Poladian, 'Numerically efficient modal decomposition approach to self-writing processes,' J. Opt. Soc. Am. A **14**, 2180 – 2189 (1997).

[26] T. M. Monro, P. D. Miller, C. M. de Sterke and L. Poladian, 'Self-similar evolution of self-written waveguides,' Opt. Lett. **23**, 268 – 270 (1998).

[27] T. M. Monro, L. Poladian and C. M. de Sterke, 'Analysis of self-written waveguides in photopolymers and photosensitive materials,' Phys. Rev. E **56** (1998).

[28] T. M. Monro, L. Poladian and C. M. de Sterke, 'Analysis of self-written waveguide experiments,' J. Opt. Soc. Am. B (1999).

[29] A. S. Kewitsch and A. Yariv, 'Nonlinear optical properties of photoresists for projection lithography,' Appl. Phys. Lett. **68**, 455 – 457 (1996).

[30] T. M. Monro, C. M. de Sterke and L. Poladian, 'Self-writing a waveguide in glass using photosensitivity,' Opt. Comm. **119**, 523 – 526 (1995).

[31] G. P. Agrawal, *Nonlinear Fiber Optics* (Academic Press, 1989).

[32] A. S. Kewitsch and A. Yariv, 'Self-focusing and self-trapping of optical beams upon photopolymerization,' Opt. Lett. **21**, 24 – 26 (1996).

[33] J. S. Aitchison, A. M. Weiner, Y. Silberberg, M. K. Oliver, J. L. Jackel, D. E. Leaird, E. M. Vogel and P. W. E. Smith, 'Observation of spatial optical solitons in a nonlinear glass waveguide,' Opt. Lett. **15**, 471 – 473 (1990).

[34] E. Hecht, *Optics* (Addison-Wesley, Reading, 1987).

[35] P. R. Graves-Morris, *Padé Approximants* (The Institute of Physics, London, 1973).

[36] M. E. Fisher, *Reports on Progress in Physics*, vol. XXX (II) (The Institute of Physics, London, 1967).

[37] G. W. Blumen and J. D. Cole, *Similarity Methods for Differential Equations* (Springer Verlag, 1974).

[38] S. An and J. E. Sipe, 'Universality in the dynamics of phase grating formation in optical fibers,' Opt. Lett. **16**, 1478 – 1480 (1991).

[39] S. V. Manakov, 'Propagation of ultrashort optical pulse in a two-level laser amplifier,' Sov. Phys. JETP **56**, 37 – 44 (1982).

[40] C. Menyuk, D. Levi and P. Winternitz, 'Self-similarity in transient stimulated raman scattering,' Phys. Rev. Lett. **69**, 3048 – 3051 (1992).

[41] J. S. Aitchison, A. M. Weiner, Y. Silberberg, D. E. Leaird, M. K. Oliver, J. L. Jackel and P. W. E. Smith, 'Experimental observation of spatial soliton interactions,' Opt. Lett. **16**, 15 – 17 (1991).

[42] D. Marcuse, *Theory of Dielectric Optical Waveguides* (Academic Press, 1991).

[43] A. W. Snyder and J. D. Love, *Optical Waveguide Theory* (Chapman and Hall, 1983).

[44] T. M. Monro, D. Moss, M. Bazylenko, C. M. de Sterke and L. Poladian, 'Observation of self-trapping of light in a self-written channel in photosensitive glass,' Phys. Rev. Lett. **80**, 4072 – 4075 (1998).

[45] M. Bazylenko, C. V. Poulsen, A. Bjarklev and O. Poulsen, 'Photosensitivity of ge-doped silica deposited by hollow cathode PECVD,' Elect. Lett. **32**, 1198 – 1199 (1996).

[46] J. Canning and M. Sceats, 'Spatial distribution of red luminescence in UV-processed germanosilicate preforms,' Opt. Lett. **19**, 1119 – 1121 (1994).

[47] E. M. Dianov, V. M. Mashinsky, V. B. Neustruev, O. D. Sazhin, V. V. Brazhkin and V. A. Sidorov, 'Optical absorption and luminescence of germanium oxygen-deficient centers in densified germanosilicate glass,' Opt. Lett. **22**, 1089 – 1091 (1997).

[48] W. J. Tomlinson and E. A. Chandross, 'Organic photochemical refractive index image recording system,' in *Advances in Photochemistry* (Eds. J. J. N. Pitts, G. S. Hammond and K. Gollnick) (Wiley, 1985), vol. 12, 201 – 281.

[49] C. Meneghini and A. Villeneuve, 'Self-writing channel waveguides in As_2S_3 thin films by two-photon absorption,' in *Nonlinear Guided Waves & Their Applications* (Optical Society of America, Washington DC, 1998), vol. 5 of *OSA Technical Digest Series*, 32 – 34.

[50] C. Meneghini and A. Villeneuve, 'As_2S_3 photosensitivity by two-photon absorption: holographic gratings and self-written channel waveguides,' J. Opt. Soc. Am. B **15**, 2946 – 2950 (1998).

[51] K. Tanaka, N. Toyosawa and H. Hisakuni, 'Photoinduced bragg gratings in as_2s_3 optical fibres,' Opt. Lett. **20**, 1876 – 1878 (1995).

[52] S. Shoji and S. Kawata, 'Optically-induced growth of fiber patterns into a photopolymerizable resin,' Appl. Phys. Lett. **75**, 737 – 739 (1999).

[53] D. Homoelle, S. Wielandy, A. L. Gaeta, N. F. Borrelli and C. Smith, 'Infrared photosensitivity in silica glasses exposed to femtosecond laser pulses,' Opt. Lett. **24**, 1311–1313 (1999).

[54] R. W. Boyd, *Nonlinear Optics* (Academic Press, 1992).

[55] A. Barthelemy, S. Maneuf and C. Froehly, 'Propagation soliton et auto-confinement de faisceaux laser par non linearité optique de Kerr,' Opt. Comm. **55**, 201 – 206 (1985).

[56] W. Torruellas, Z. Wang and C. R. Menyuk, 'Observation of two-dimensional spatial solitary waves in a quadratic medium,' Phys. Rev. Lett. **74**, 5036 – 5039 (1995).

[57] M. Segev, B. Crosignani and A. Yariv, 'Spatial solitons in photorefractive media,' Phys. Rev. Lett. **68**, 923 – 926 (1992).

[58] G. Duree, J. L. Shultz, G. Salamo, M. Segev, A. Yariv, B. Crosignani, P. DiPorto, E. Sharp and R. Neuraonkar, 'Observation of self-trapping of an optical beam due to the photorefractive effect,' Phys. Rev. Lett. **71**, 533 – 536 (1993).

[59] G. Duree, G. Salamo, M. Segev, A. Yariv, B. Crosignani, P. DiPorto and E. Sharp, 'Dimensionality and size of photorefractive spatial solitons,' Opt. Lett. **19**, 1195 – 1197 (1995).

[60] M. Morin, G. Duree, G. Salamo and M. Segev, 'Waveguides formed by quasi-steady-state photorefractive solitons,' Opt. Lett. **20**, 2066 – 2068 (1995).

[61] D. N. Christodoulides and T. H. Cosjun, 'Diffraction-free planar beams in unbiased photorefractive media,' Opt. Lett. **21**, 1460 – 1462 (1996).

[62] M. Segev, G. Valley, B. Crosignani, P. DiPorto and A. Yariv, 'Steady-state spatial screening solitons in photorefractive materials with external applied field,' Phys. Rev. Lett. **73**, 3211 – 3214 (1994).

[63] M. F. Shih, M. Segev, G. C. Valley, G. Salamo, B. Crosignani and P. DiPorto, 'Observation of two-dimensional steady-state photorefractive solitons,' Elect. Lett. **31**, 826 – 827 (1995).

[64] Z. Chen and M. Segev, 'Observation of incoherently coupled photorefractive spatial soliton pairs,' Opt. Lett. **21**, 1436 – 1438 (1996).